The Pennsylvania State University

The Graduate School

The Harold and Inge Marcus Department of Industrial and Manufacturing Engineering

IMAGE-GUIDED ADDITIVE MANUFACTURING

A Thesis in

Industrial Engineering and Operations Research

by

Aniket Sunil Sakpal

Submitted in Partial Fulfillment

of the Requirements

for the Degree of

Master of Science

May 2017

The thesis of Aniket Sunil Sakpal was reviewed and approved* by the following

Hui Yang

Associate Professor of Industrial and Manufacturing Engineering

Thesis Advisor

Russell Barton

Professor of Supply Chain and Information Systems and Industrial Engineering

Janis Terpenny

Professor of Industrial and Manufacturing Engineering

Department Head, Industrial and Manufacturing Engineering

*Signatures are on file in the Graduate School

ABSTRACT

Additive manufacturing is often a complex undertaking involving interaction between an energy source, feedstock, and substrate. Many independent process variables such as travel speed, feedstock flow pattern, laser power, chamber gas, etc. contribute significantly to the overall build quality of the component. Any fluctuation in these process variables affects the quality of the final part inducing defects and results in non-conformance to dimensional tolerance, microstructure, and properties. A wide variety of sensor data and analysis have been used for process monitoring and quality control of the additive manufacturing processes. Sensor feedback enables to form a correlation between the variation in process parameters contributing to the changes in the final build quality. This thesis presents new methods of multifractals and uncorrelated multilinear principal component analysis of additive manufacturing images for process machine modeling and defect characterization in the additive manufacturing based components. First, we simulated the classical defects encountered in additive manufacturing on a set of in-situ images of AM process. Second, we applied the proposed methodologies to the in-situ images and extracted the parametric features correlating to the defects and irregularities induced on the images. Third, we checked the statistical significance of the parametric features from the images of defects to the images of control quality. In the end, we compared both the methodologies for successful detection and characterization of defects/discontinuities emerged in the additive manufacturing processes.

Keywords – Additive Manufacturing, Defects, Simulation, Multifractals, UMPCA

TABLE OF CONTENTS

LIST OF TABLES

TABLE OF FIGURES

Acknowledgements

I owe my deepest gratitude to my advisor, Dr. Hui Yang, for all guidance and mentoring offered to me throughout my graduate studies. He has always inspired, and encouraged me, and without his support, I would not have been able to achieve my graduate career goals. He brings best out of the student, and it was honor and privilege to work under him. I am thankful to Prof. Russell Barton for agreeing to be my reader for this thesis. I am grateful for his valuable contribution to improving the quality of research, and I have learned a lot from him during my graduate years. He is an amazing person, and his interaction with students make them feel at ease. I would like to thank Prof. Ted Reutzel from Applied Research Lab for providing me data that was the foundation for this research. I would also like to acknowledge the valuable contributions of Dr. Abdalla Nassar and Steve Brown from ARL at Penn State for building the imaging system and Gabrielle Gunderman, a PSU student who assembled the data used in this experiment.

I am indebted to my lab colleagues Chen Kan, Bing Yao for helping wholeheartedly for the research and development of this thesis. I am thankful to my friends who also have become my family in U.S., Siddharth, Aakash, Goutham, Shrey, and Habeeb for all the support, love, and memorable moments in one of the best phases of my life.

Most of all, I want to thank my parents, Sunil Sakpal and Archana Sakpal, and my brother, Rohan Sakpal who have always supported me in pursuing my goals and ambition. Your love, teachings, and sacrifices made me what I am today.

CHAPTER 1.   INTRODUCTION

Additive manufacturing processes work on the principle of adding successive layers of material to make an object of the desired shape. This concept changed the traditional assumptions of building an object by removing the mass through the object using machines such as CNC drilling, milling, etc. AM processes have superiority over many traditional processes. AM methodologies do not involve jigs, molds, fixtures, or any special apparatus, which decreases overall operation time of the process. AM have spread its wings to the field of toolmaking, dental, medical, and aerospace after been limited to models and prototypes in initial years. Complex shapes can be built selectively as per their structure and geometries which were challenging in the past. AM technology offers Near-net shaping where initial production of the item is close to the final (net) using less material thereby producing less waste. Because of these factors, commercial exploitation of AM has been increased, and many industrial sectors started seizing the opportunity. AM technology can reduce total environmental impact up to 70% than conventional machining [1]. Even cost benefits are in line with benefits using the AM technology. Different studies have claimed 50-80% weight reduction in an aircraft is possible if metal brackets are developed using AM methodologies amounting to yearly saving of millions in fuel costs[2]. GE has been achieving benefits of AM technology with reduced operations time and money without sacrificing performance [3]. A wide range of materials can be developed using additive manufacturing including metals, plastics, alloys, composites, etc.

1.1　Additive Manufacturing

Additive manufacturing, also known as 3D printing, refers to the process of building an object by adding layers of material one by one in all three directions. The material can be a plastic or metal. The techniques used in the additive manufacturing of metals are slightly different from those performed in plastics. The technologies in the metals-based additive manufacturing have evolved using welding and cladding (walls) processes that have been around for decades. The advantage of AM is the development of ready-to-use part from design stage in less time and number of manufacturing steps. A set of machine instructions follows the CAD (Computer-Aided Design) object transforming the surface geometries of the virtual part into a set of tool paths. Mass-efficient designs with intricate geometries can be developed directly from the computer-aided designs, without the design of constraints of conventional processes. Additive manufacturing involves lots of complexity involving hundreds of individual laser or electron-beam deposits in the process. Significant interaction between an energy source, substrate, and feedstock lead to many process variables that contribute to the overall build quality of the product. These limitations have given rise to the need for sensing and control strategies for achieving sophistication of the overall additive manufacturing techniques.

1.2　AM Processes and Subsystems

American Society for Testing and Materials (ASTM) standard F2792 defines additive manufacturing as "the process of joining materials to make objects from 3-D model data, usually layer upon layer, as opposed to subtractive manufacturing technologies" [4]. Additive manufacturing processes vary in types and differ depending on the kind of

material and machine technology used. Fully-dense parts can be built using additive manufacturing processes in one of two categories: (i) directed-energy deposition and (ii) powder-bed fusion (ASTM F42 Committee, 2012)[5]. Both the process differs in the material used in the process. In the directed-energy deposition, powder or wire is fed into a molten pool on top of the substrate. In latter, electron beam or laser is scanned over a bed of powder on top of the substrate. The subsystem of both categories is similar apart from feeding material. It consists of an electron beam or laser, a beam delivery system, motion controls, feedstock delivery system, and environmental controls. Figure. 1 and 2 show the AM categories of Directed Energy Deposition and Powder bed fusion. Figure 1.2:3 shows AM and its subsystems.
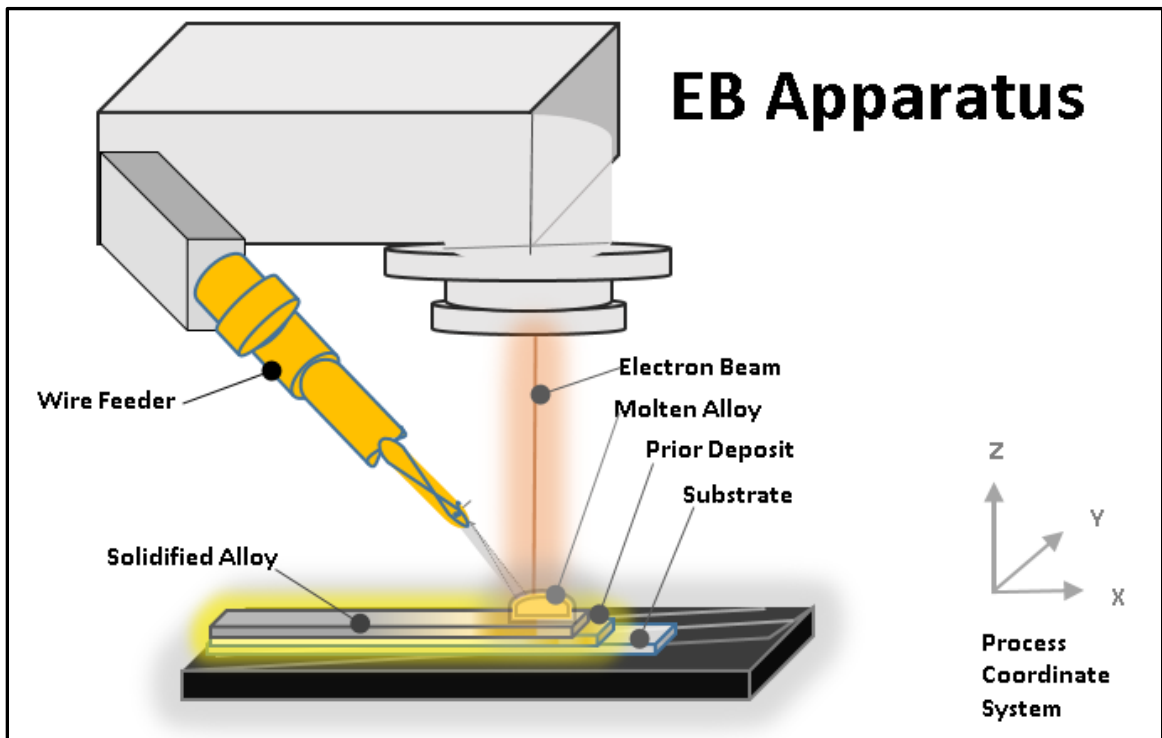
Figure 1.2:1: Electron beam, wire-fed DED system
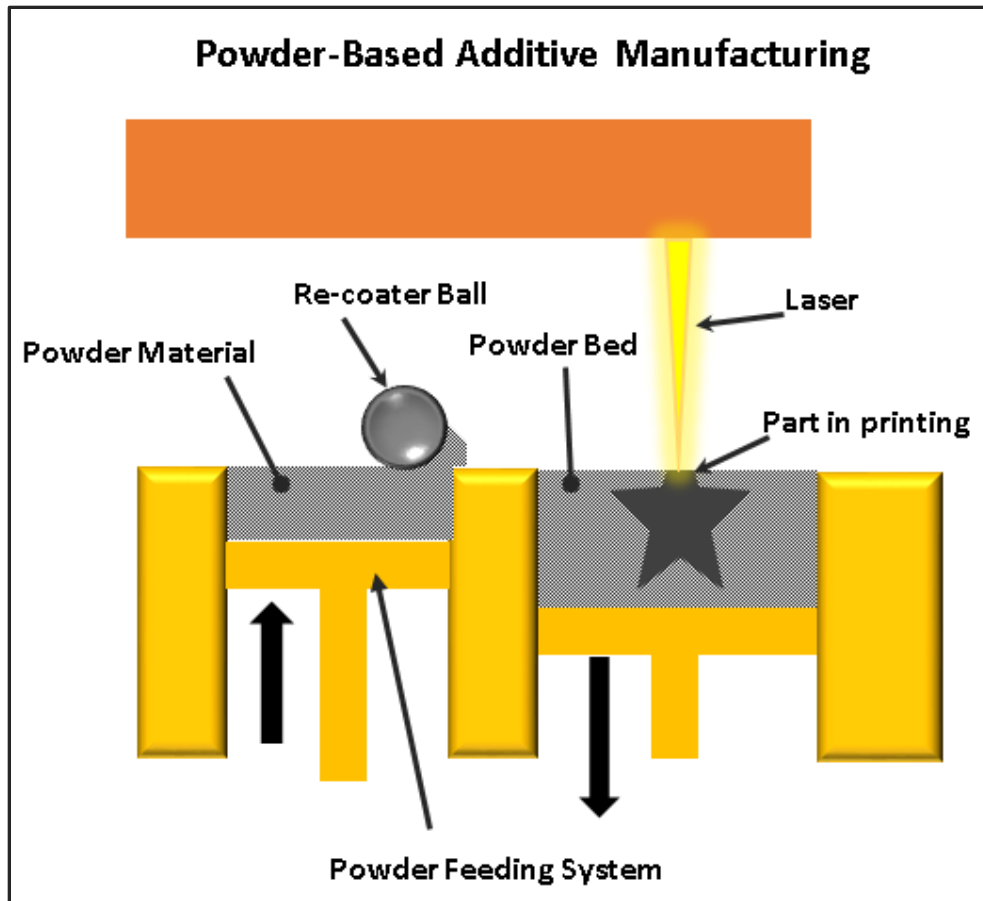
Figure 1.2:2 Powder-bed additive manufacturing
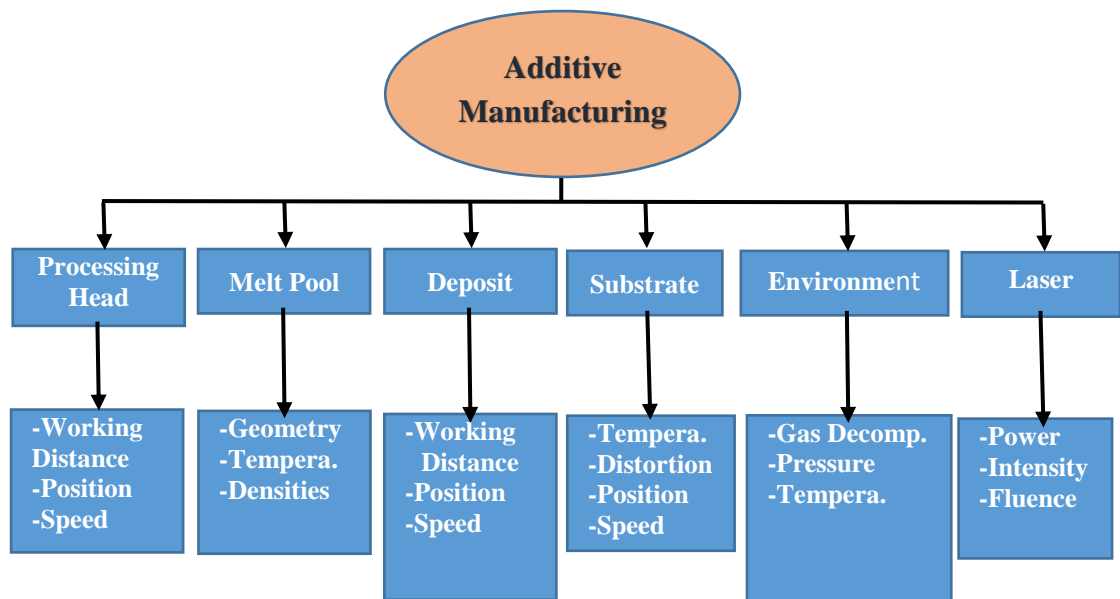
Figure 1.2:3 AM and its subsystems

1.3 Sensing and Control of Machine Variables

Additive manufacturing solves many shortcomings that come with traditional processes, but AM has its own complications which need to be monitored for better quality and accuracy. Some of the early obstacles of the AM processes identified by the researchers persists today (porosity, cracking, thermal management). This can be mainly attributed to lack of process monitoring and fault diagnostics systems used to manage AM operations. Many independent factors are involved in the process which poses a challenging task for achieving top-notch grade in quality and repeatability. Some of the problems arise in AM are inherent to the working of the AM principle and its supporting systems. Key process parameters can be accounted for the performance of final build quality such as strength, surface roughness, dimensional tolerance, and structural properties. For illustration, discontinuities may appear in building direction if the melted matter is unable to fuse properly due to low laser scan[6]. In powder bed fusion, uneven melt pool temperature affects the microstructure and structural properties of the object. If the key performing variables are identified, these variables can be adequately monitored and controlled to improve the quality features of the object. Sensing and feedback control can be employed for each of these variables. These can provide us the information on instabilities in the subsystems causing non-conformance of the final build quality. For such capabilities in the system, sensor technologies are on the rise to effectively monitor the parameters influencing the quality and accuracy of the produced components [5]. A key methodology in process monitoring and fault diagnostics is the in-situ monitoring techniques. Although the use of in-process monitoring is common in traditional processes, AM processes are yet

to be benefited from monitoring techniques that allow in-situ detections of defects/discontinuities.

1.4 Defects/Irregularities in Additive Manufacturing Processes

Some of the early drawbacks of additive manufacturing were the formation of defects and discontinuities which persist today. The building process in most additive manufacturing technologies relies on a continuous layer-by-layer addition process. So, the breakdown of 3D design into the 2D layer is a principal drawback of AM. Discontinuities may appear in all building directions because of the layer-by-layer addition process. Most typical defects are built up between the internal layers of the components during AM processes. In AM, pores are most susceptible to fatigue cracks than structural instabilities [7]. Cracks extending to the component surface due to pores affect fatigue life and result in breakages. Insufficient laser power in powder bed processes results in the formation of gas pores due to partially un-melted powders [6]. Over-melting causes disorder within the melt pool and hence, uncontrolled evaporation which give rise to gas pores between the layers of material. Therefore, there is a need to develop a better correlation between process parameters and the defects found within the layers of AM based component. Some of the typical defects are shown in Table 1.

Sensor methodologies can provide us valuable feedback for better monitoring of the AM process and give insights on the failure mode and effect analysis. But the process monitoring and control techniques allowing to detect the discontinuities in the AM processes have not been fully developed. Researchers have been proposing and investigating new forms of mechanism and sensing techniques which, when integrated with

AM system will allow the discontinuities to be detected, monitored and successfully characterized for realizing the full potential towards process monitoring and fault diagnosis.
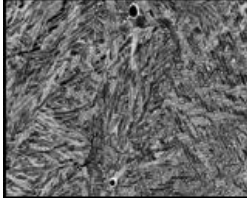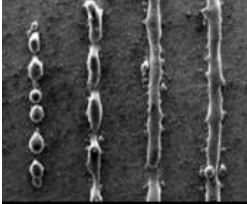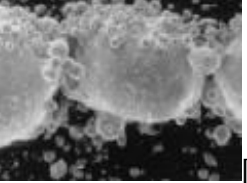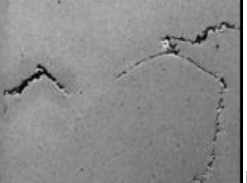
Material Discontinuities	Description	Defect Image
1. Gas Pores	Trapped gases causing pores within the layers	[8]
2. Elongated Pores	Incomplete fusion of powder particles causing irregular pore	[8]
3. Balling	Large spherically shaped formation due to excessive melting	[9]
4. Infused Powder	Insufficient laser power develops unfused powder regions	[10]
5. Cracking	Crack defect extending in multi-direction relieving stress	[11]

Table 1. Summary of Defects/ Discontinuities in AM processes

1.5 Motivation and Objective of the Proposed Research Related to Additive Manufacturing

Chapter 5 of this research thesis describes the successful detection and classification of defects in the AM processes through image based sensors. This is achieved through the development of methodologies that differentiates the images having defects from the images of in-control quality. These methods are as follows:

1. Multifractal analysis of images describing the heterogeneity in the additive manufacturing systems through features and parameters of multifractal spectrum correlating to the irregularities and defects in the images.

2. Uncorrelated multilinear principal component analysis extracting the principal component features from the multi-dimensional image data of additive manufacturing that points to the irregularities and defects in the images.

These methodologies can help in in-situ process monitoring of additive manufacturing. This thesis is organized as follows: Chapter 2 describes the review of related literature. The research methodology and experimental studies developed for the process monitoring and defect detection of the additive manufacturing process are detailed in Chapter 3. Chapter 4 outlines the design of experiments, experimental set-up and simulation strategies used for process modeling and defect characterization in this research. Chapter 5 summarizes the results and discussion of this investigation. Finally, Chapter 6 describes the potential future research for application of these methodologies for real-time, online process monitoring.

CHAPTER 2.   LITERATURE REVIEW

This chapter describes the research background and reviewed the literature relating to in-situ process monitoring of defects in additive manufacturing.

2.1   Review of the Literature Relating to In-situ Process Monitoring in Additive Manufacturing

Here are reviewed typical defects which occur in the additive manufacturing processes as well as the sensor methodologies used to detect such defects in the past and identify shortcomings in the current state of sensor methodologies.

2.1.1   Process Errors and Defects
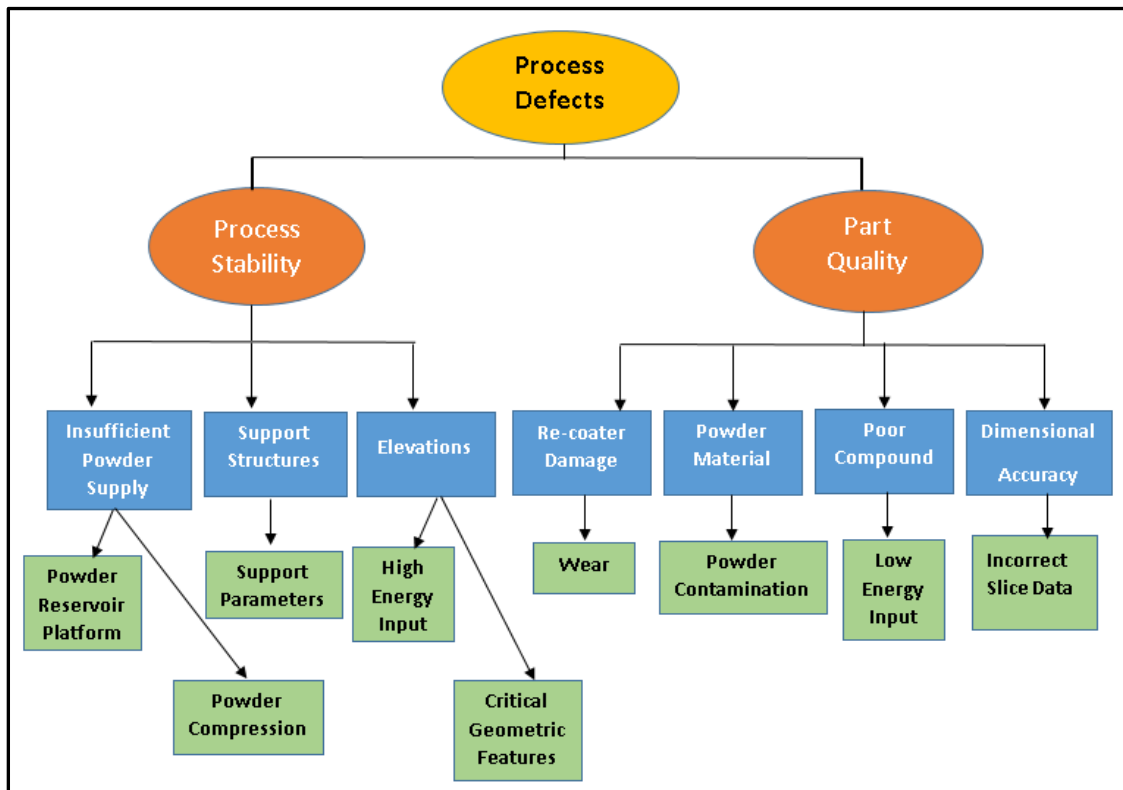
Figure 2.1:1 Typical process errors in AM processes by influence, type and cause [12]

Many dependent and independent parameters are involved in AM processes which influence the characteristics of final build component. Processing parameters such as laser power, scanning speed, hatch distance, etc. govern AM processes. Van Elsen list over fifty parameters for laser-PBF processes [13]. The fundamental mechanism of "defect" or irregularities forming into the powder bed additive manufacturing have been addressed as early as by Kruth et. al [14]. Figure 2.1:1 shows the typical process errors encountered in AM processes.

2.1.2   Pore Defects

Variety of defects and irregularities are known to occur in AM processes, typical are the ones that are built up between the internal layers of the components, for e.g. elongated pores forming between layers or gas pores within the layer. Attar et al. showed that insufficient laser power in powder bed processes results in the formation of gas pores due to partially un-melted powders [6]. It revealed that low laser power had a significant influence on pore formation. When the laser power was less than 100W, a significant number of un-melted particles and porosities were developed, as shown in Figure 2.1:2. This phenomenon was caused by incomplete melting of the powders due to insufficient laser power and unbalanced viscosity of melt pool. It was also shown over-melting due to high laser power can result in gas pores within the material due to increased stress and excessive evaporation. Thus, the processing parameter of laser power as the main reason for the creation of this discontinuities/defects.
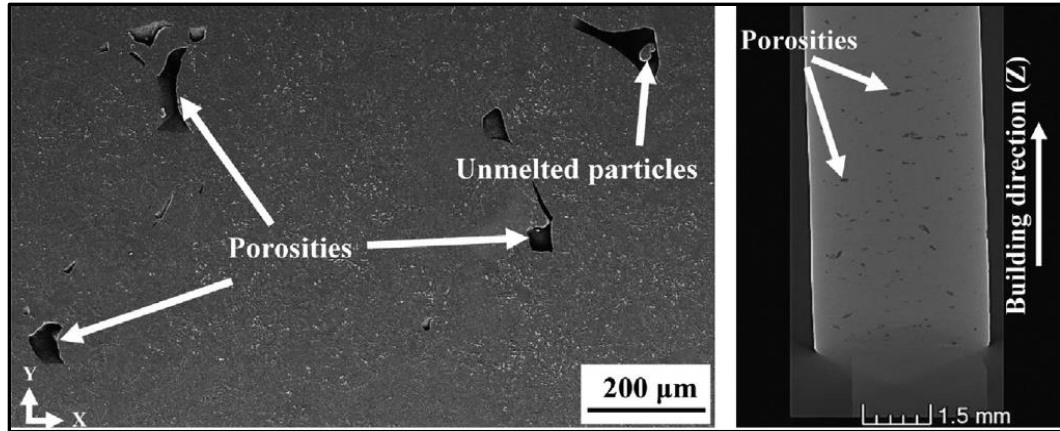
Figure 2.1:2 Defects of porosity and un-melted particles due to low laser power [6]

Tammas-Williams et al. performed X-ray computed tomography (XCT) to reveal that the variation in hatching/scanning regime is the reasons for the formation of voids and discontinuities[8]. Most pores were found to be small spherical gas pores, attributed to the lower energy density and low focused beam used. Increasing the power of beam focus or the energy density resulted in the reduction in gas porosity level. Irregularly shaped pores were primarily found in the inter-build region and probably caused by insufficient fusion in powder particles. Some of the images of the pores discontinuities developed in the experiment are shown in Figure 2.1:3
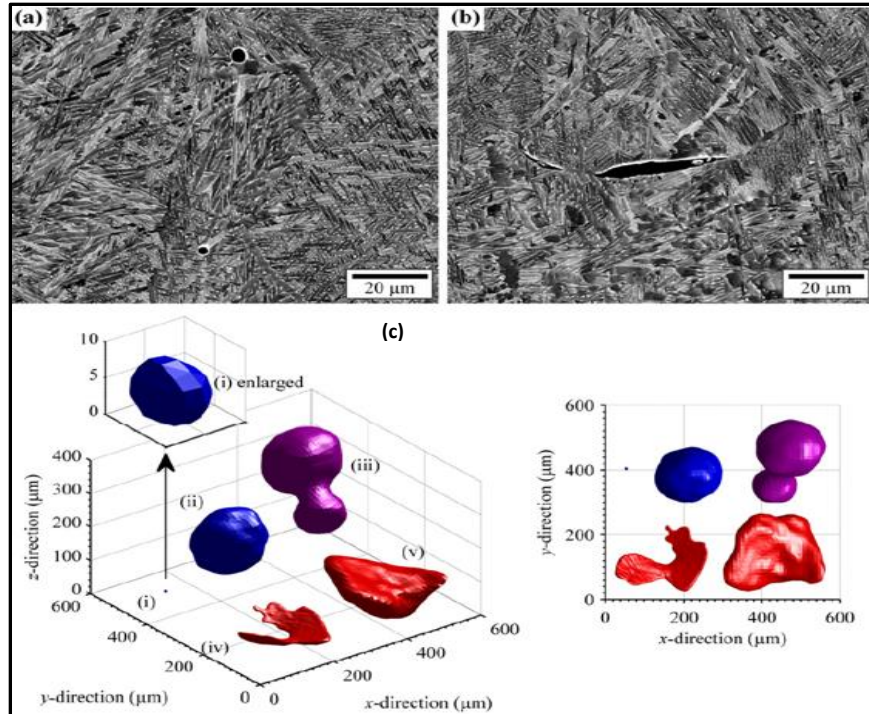
Figure 2.1:3 Pore defects in AM processes identified by Tammas et.al, (a) two round pores, (b) irregular pore, (c) pores structure and sizes in detail [8].

2.1.3 Balling Defects

In high laser power environment, another defect called "balling" of powder emerge when powder material fused together excessively to form spheres that rise above the layer thickness, due to the oxidation process in the build chamber. This phenomenon creates a discontinuity in the subsequent layers making the surface uneven. Gu et al. revealed similar event of balling happened in stainless steel powders in a lower power setting[15]. Balling defects were divided into two types: One formed due to insufficient laser energy input, and the second by molten pool splashing under high scan speed. Childs et al. performed experiments to study the effects of single laser track on balling due to different scan speed and laser power [16]. Single scan paths under varying laser powers are shown in Figure 2.1:4 (c). Li et al. revealed that the balling incidents could be controlled by lowering the

oxygen content in the chamber environment [9]. Development of a smooth melting surface demands lower oxygen content to prevent balling defects in SLM. A higher O_2 content of 2% and 10% will initiate the balling event, as schematically shown in Figure 2.1:4 (a) and (b).
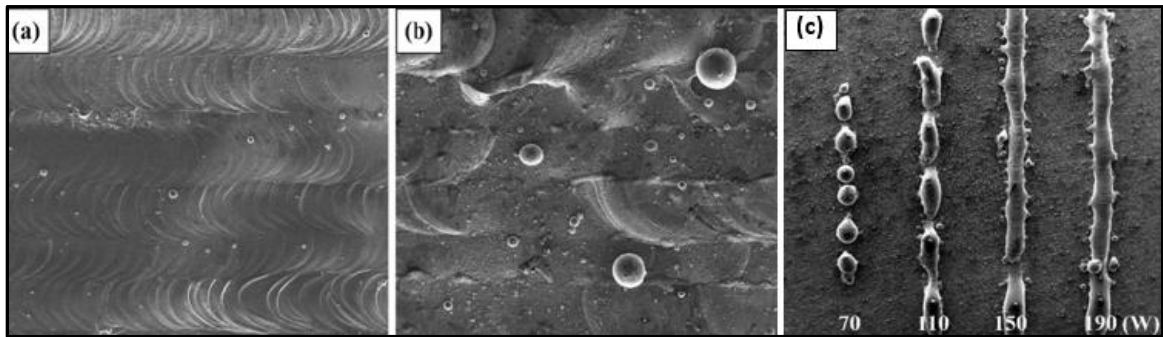
Figure 2.1:4 Balling phenomenon with varying O_2 contents in chamber environment: a). 0.1% O_2 content; b). 2% O_2 content; c). single scan paths under different laser powers[9]

2.1.4   Re-coater Damage affecting Powder Layer

S. Kleszczynski et al. showed process stability could be at risk due to the collision of the re-coater blade and curled areas [12]. Melting and solidification in high cooling environment develop residual stresses causing plastic deformation within the layer. Support structures are necessary to counteract deformations and prevent the process from stopping. Heat induction is another reason for using support structures since the conductivity of metal powders is not same as solid metal. Unless the heat induced is not relieved in building platform, balling effects appear Fig 2.1:5 (a). Residual stresses building up within the bed causes inconsistencies in the layer called 'curling up.' These areas of increased thickness can affect the subsequent distribution of the powder layer as in Figure 2.1:5 (b). To mitigate such effects, silicon blades can be used for spreading the powder layer but they have short life and erode quickly.
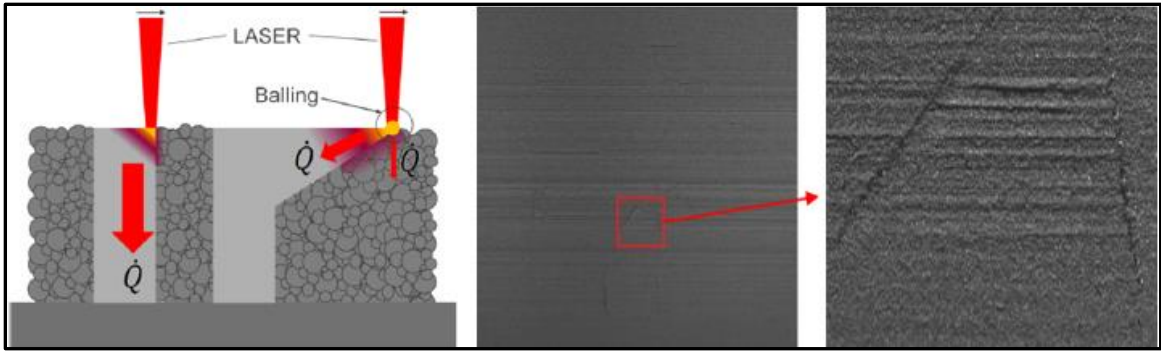
Figure 2.1:5 a) Balling event due to insufficient heat conduction, b) visible horizontal lines caused by a damaged recoater blade [12]

2.1.5 Crack Defects

Product quality is affected by the hot cracks defects in AM which depend on the powder material and heat input density. Most materials used in AM show good welding characteristics and hence, assigned to ductile metal alloys. The problem arises when the different concentration of metal powder or powder contaminations are used and thereby pose such defects. This exerts the use of specific ratios between width and distance melt traces in such processes. The width of melt traces depends on many factors such as laser beam diameter, laser scanning velocity, etc. If the gap between melt traces (hatch distance) – is too big as in Figure 2.1:6 (a), melt traces will be deranged causing porosities and poorer mechanical properties [12]. Wang et al. performed acoustic emission testing to reveal crack defects in powder-DED as one shown in Figure 2.1:6 [11]. The experiment presented four typical forms of the cracking defect: (1) the slag cracks occurring at the grain boundary, (2) The cracks generating at the combining sites of coating and substrate. (3) The cracks forming at the bonding zone. (4) The cracks resulted from manufacturing.
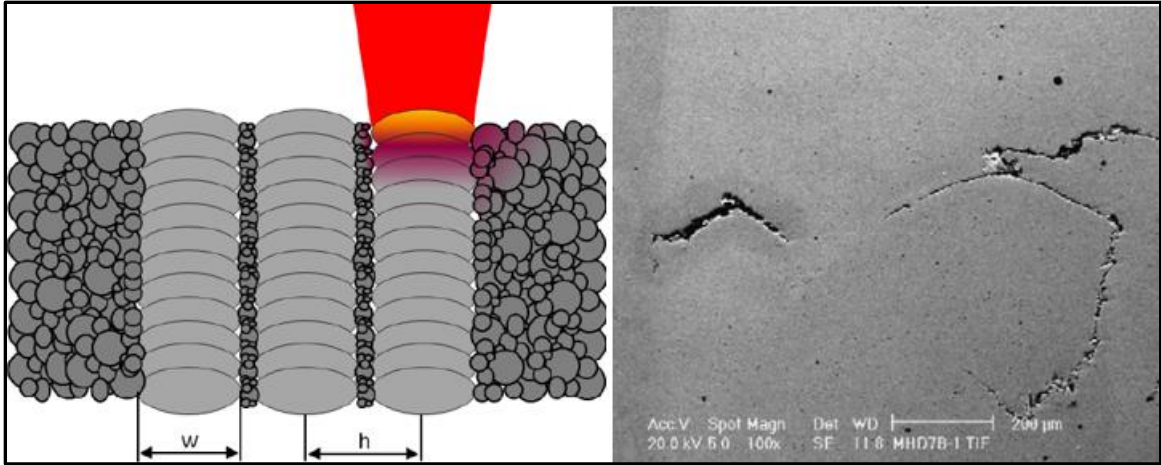
Figure 2.1:6 (a) Poor composite weld seams due to variation in ratio of hatch distance h and width w [12] (b) the cracks extending in multi-directions [11]

2.2 Process Monitoring and Sensor Methodologies

Process Monitoring of the AM process relies on the data collection methods capturing the process-related features pointing to the sources of inaccuracies and defects that can lead to failure. Process-related data will be much more effective if the monitoring techniques are real-time so the information related to the errors and defects can be effectively understood. Monitoring techniques that detect material discontinuities during the build in AM processes would help in the tight control of the process characteristics as every layer of the build could be assessed for defects and flaws and give room for correctional strategies. This possibility can provide information on the process parameters and their ranges for building parts with better quality and accuracies. There have been numerous effort to address the process monitoring of AM processes to enhance the part quality [17]. Most of the research within the process monitoring and control of temperature centered around on pyrometry, which is the non-contact measurement of the temperature of a body based on its emitted thermal radiation. Photodiodes and digital cameras are most favored

type of pyrometers used in AM. As opposed to pyrometers, a thermocouple is a device that conducts contact measurement of temperature. Figure 2.2:2 shows the typical visual inspection system in AM for powder surfaces.
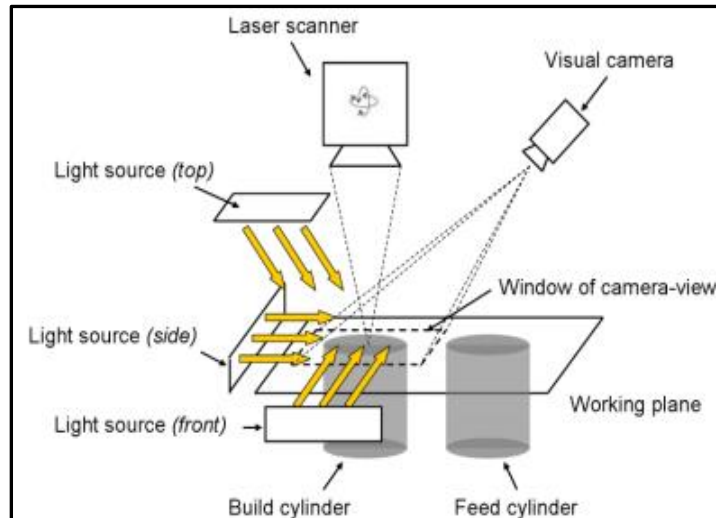
Figure 2.2:1 Visual inspection system for monitoring powder layer surfaces [18]

2.2.1   In-situ Methodologies of Process Monitoring

A key methodology in process monitoring and control technologies is the in-situ monitoring techniques. These techniques help in closed loop monitoring and detection of defects/discontinuities through in-situ data acquisition methodology. New forms of in-situ instrumentation and methodologies are developed continuously which allows further enhancement to improve the quality of AM components [19]. Early works in-situ inspection of AM processes utilized an in camera or photodiodes based setups. Early works of Kruth et al. performed process monitoring by combining a visual inspection camera equipment and a melt pool monitoring system [18]. The system inspected the decomposition of powder layer for any instabilities in the powder recoating system causing surface distortions in the powder bed after scanning. These irregularities pass on to

subsequent layers and cause high surface roughness. A light source was used in the process chamber to brighten the horizontal lines caused by the damaged powder coating system. An analysis of gray values was used for detection of powder bed irregularities as shown in Figure 2.2:2. The high standard deviation in pixel values indicated the wear and instability of the recoater blade. This arrangement can be used to detect irregularities in the system and corrective action can be implemented at the first layer and prevent other layers of powder from being affected.
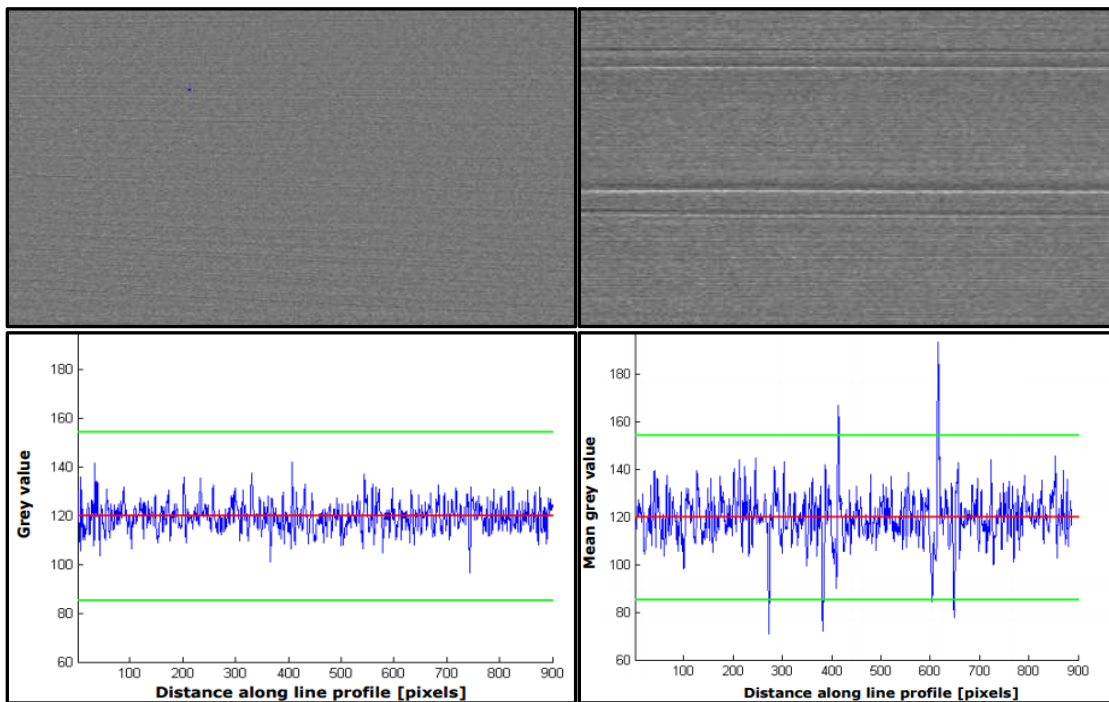
Figure 2.2:2 Image of proper quality powder bed, (b) illuminated image of powder bed with irregularities, (c) illustration of pixel values with mean 120 and standard deviation 5.75 for proper quality and (d) illustration of pixel values with mean 120 and standard deviation 10 for irregular powder bed [18]

Berumen et al. showed the use of scan head and semi-transparent mirror for transmitting the radiation by the melt pool and image to high-speed camera respectively [20]. The experiment showed that the photodiode sensor could distinguish temperature gradients across build area and a camera with significant resolution could acquire the melt pool

17

features illustrated in Figure. 2.2:3. Predefined limits of temperature ranges for melt pool could be possible to regulate with the help of closed loop feedback and control. This enables to keep the material from overheating and causing gas pores.
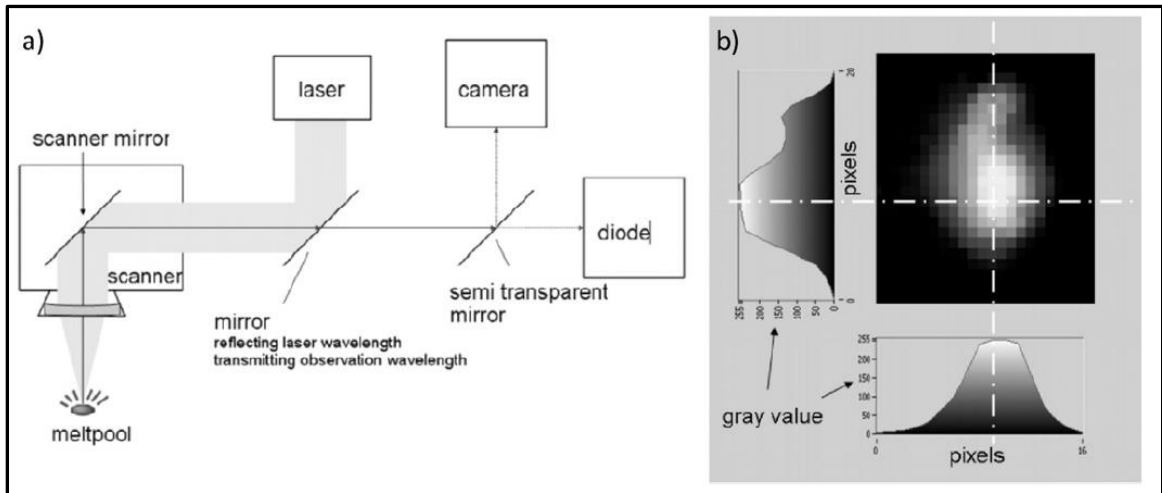
Figure 2.2:3 (a) Schematic representation of camera and photodiode (b) camera system showing different intensity by Berumen et al. [20]

Furmoto et al. used a simple system of high-speed cameras [21]. The system monitored the powder bed during irradiation by the vertically installed camera above the powder bed. The deviation in powder layer thickness was captured by camera images lighten by a metal halide lamp. Pavlov et al. used a two-wavelength pyrometer in-line with the optical unit of a laser-PBF Phoenix PM-100[22]. This arrangement helped to monitor hatch distance for powder thickness and the catch any deviations in powder layer thickness, as shown in Figure 2.2:4. Through the experiment, it was found that the readings are affected due to heat build up in the previously melted layer. Islam et al. used pyrometry to assess the reasons of balling through visual inspection system [23]. It showed that minimum heat inputs in the range 1400 J mm-3 to 1700 J mm-3 reduces balling defects, and cooling rates not causes any effects of the balling phenomenon.
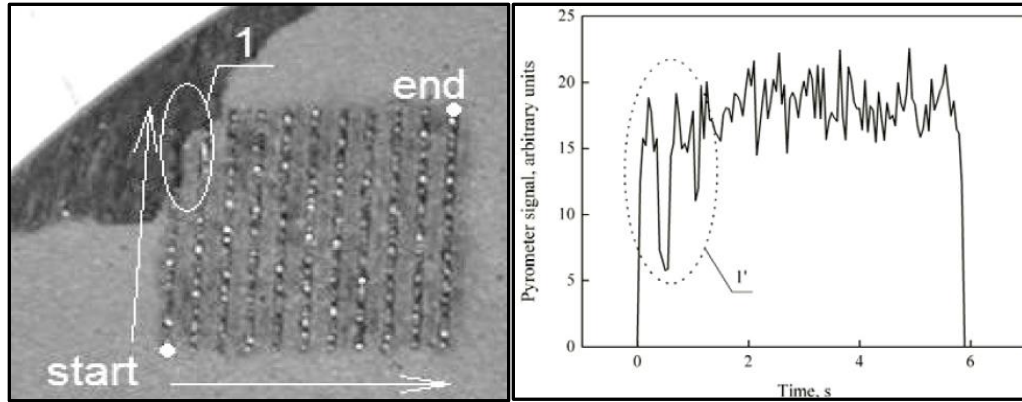
Figure 2.2:4 (a) Mismatch in the powder layer of first two tracks; (b) pyrometer signal depicting irregularity in the powder layer [22]

Rodriguez et al. used an Infra-Red camera into an Arcam A2 electron beam-PBF machine, shown in Figure 2.2:6, to assess surface temperature profiles for each powder layer [24]. The profile values extracted can be used to rectify the performance settings for subsequent layer. ThermaCAM Researcher analyzes the images to measure the emitted radiation from the surface and transforming to a relative temperature reading. Defects caused by "over-melting" during the AM process could be distinguished from the generated Infra-Red image, shown in Figure 2.2:5 (b).
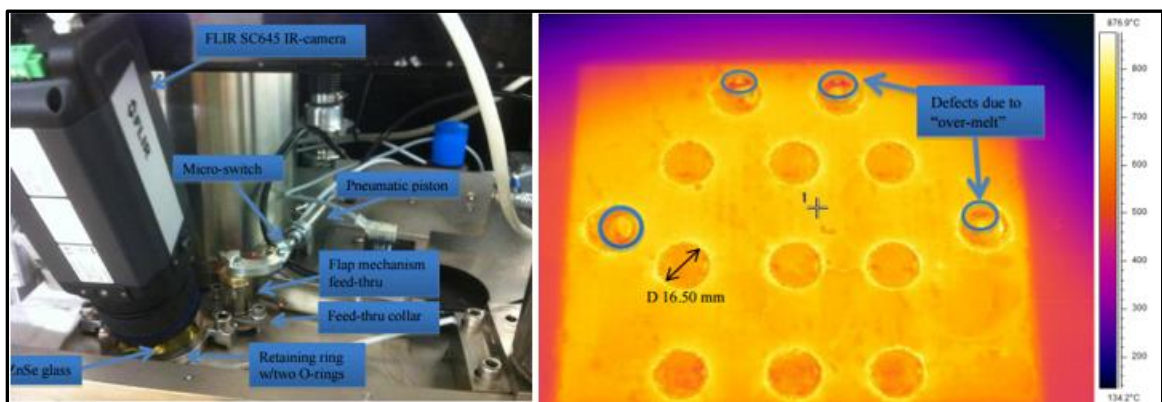
Figure 2.2:5 (a) Showing ArcamA2 build chamber with Infra-Red camera and (b) corresponding image in Infra-Red settings with defects by Rodriguez et al. [24]

High-speed cameras with large view has given rise to identification method to diagnose irregularities in the powder bed due to re-coater damage and over-processing causing parts to curl up in AM. Although the defects and irregularities in AM can be manually detected, closed-loop monitoring and automatic defect detection is still out of reach in most in-situ methodologies and yet to be attained.

2.3   Shortcomings in the existing methodologies

Most of the previous work were limited to the detection of defects in additive manufacturing but lack the characterization and classification of defects. Standard image processing techniques that detect defects in the images involves three general phases of pre-processing, enhancement and display, and information extraction. Pre-processing techniques such as image enhancement, filters, edge detection, noise removal, etc. are needed before reaching an output of either an image or a set of parameters related to the image. Further steps necessitate characterizing the defect through feature extraction as typical defects such as pores, balling, cracks, etc. have different shapes, sizes, and spatial arrangement. Hence above methodologies lose on computational time, resources, and several operations involved in generating results of detection and characterization of defects. In this thesis, we are proposing two methods which will not only detect but also characterize the defects without the need for any image processing techniques. It will run the original image of AM processes and detects the deviation in parameters belonging to the irregularities such as defects/discontinuities. This methodology will provide parametric features that can be correlated to the different type of defects with size, shape and spatial arrangement and hence, will be able to differentiate images of control and fault in the in-situ operations of additive manufacturing.

CHAPTER 3. RESEARCH METHODOLOGY

This chapter details the research methodology of multifractal analysis and uncorrelated multilinear principal component analysis used to detect the defect in the images of additive manufacturing.

3.1 Multifractal Analysis Approach

Lakes, oceans, mountains are often described as circular, cone, spheres but they are not. Natural patterns and shapes are so irregular and fragmented that they exhibit not simply a higher degree but entirely altogether different level of complexity[25]. Standard geometric measurements are not enough to capture their dimensions and complexity. The concept was first introduced by Mandelbrot (1977, 1983) to describe nature's complexity and thus, coined the term "fractal geometry" [26]. Many natural phenomena have an ingrained irregularity in their systems and look somewhat similar to each other at different scales, as shown in Figure 3.1:1. This scale invariant similarity is a source of simplicity in fractal geometry. Observed fractal structure remains similar under the scales of magnification or contraction. For example, components of trees such as a trunk, branches, leaves, etc. have similar patterns in their shapes, structure and spatial arrangement. This patterns under magnification are a miniscule replication of the whole: not identical, but similar in nature. Even some of the man-made structures have exhibited the property of fractal geometry and often subject to research as in Figure 3.1:1 (b). Since the advent of fractal geometry, it has been used extensively to describe the complexity of non-linear systems such as ecology, signal and image processing, soil mechanics, etc.[25][27][28].

Figure 3.1:1 (a) Natural fractal systems of exhibiting self-similar patterns [29][30][31][32](b) some other man-made fractal systems[33][34]

3.1.1 Fractal Geometry

Fractals defined by Benoit Mandelbrot as "A fractal is by definition being a set for which Hausdorff-Besicovitch dimension strictly exceeds the topological dimension." The concept of dimension is vital in fractal geometry. Dimension can be defined as "A measure of spatial extent, especially width, height, or length or can be defined as the least number of coordinates required to specify the points uniquely in space." The first fractal was discovered by a French mathematician named Gaston Julia who discovered them decades before the advent of computer graphics [35]. Julia's work was discovered by Benoit Mandelbrot. A fractal set fills the space in which it is embedded and possesses a certain degree of self-similarity with high irregularity. If we reduce the linear size of an object in

the Euclidean space $\mathbb{R}^D$ by the scaling factor ε in each spatial direction, its measure (length, area, or volume) will increase to $N = \varepsilon^{-D}$, where N is the number of measure elements needed to capture the object. This measure is captured by fractal dimension, D_F, of the set. Fractal sets have theoretical dimensions exceeding their topological dimensions and can be non-integer values. Figure 3.1:2 (a) shows an example of the Koch snowflake curve which has a non-integer dimension[36].
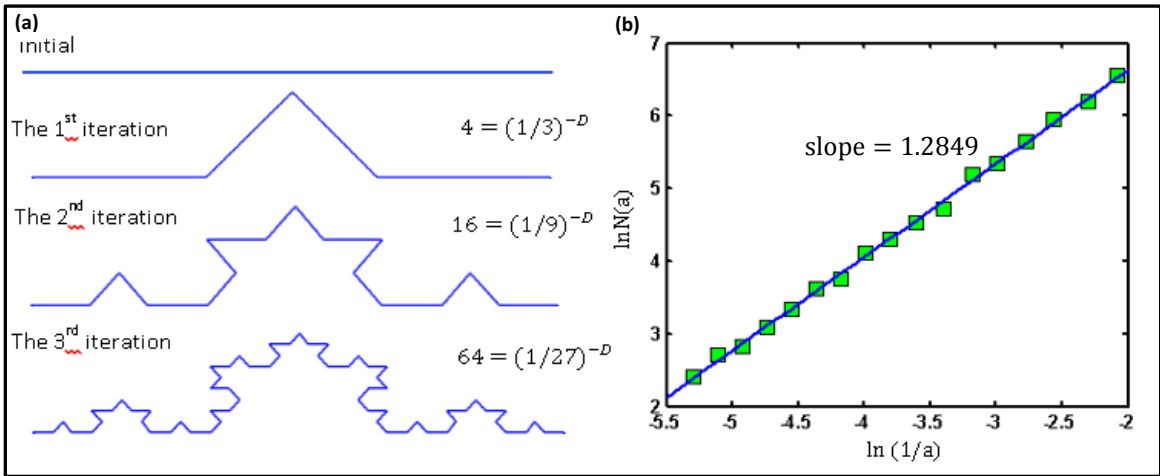
Figure 3.1:2 (a) Self-similarity and fractal dimension from Koch curve (b) plot of ln(1/a) against ln N(a) for Koch curve[37]

The Koch snowflake curve is self-similar at all scales of magnification. The Koch snowflake curve is generated by starting with a straight line, and dividing the line into three segments of equal size. Second, remove the middle part of the line and replace it with two lines that have the same length (1/3) as the remaining lines on both sides[37]. Iterating this process recursively generate the "infinitely complex" Koch curve. Fig. 3.1:2 (a) shows the first three iterations of the process. In each iteration, the length of the curve increases. However, the Koch snowflake curve is self-similar at all scales of magnification. If we follow the scaling and covering rule, the dimension of Koch curve is $D = -\log 4 / \log(\frac{1}{3}) = $

1.26. The Fig. 3.1:2 (b) shows the plot of ln N(ε) against ln(1/ε) for the Koch curve with estimated slope is approximately 1.2849, while theoretical fractal dimension is 1.263.

3.1.2 Theory of Multifractal and Mathematical Proof

Fractal geometry is advantageous in explaining complex systems using a relatively low number of parameters as in the case of Dimension D_F [37]. Compared to classical approach of image analysis, fractal and multifractal analysis are advantageous in the way of handling of irregularities [28]. Major motivation of the work is developed through the paper on multifractal characterization of soil pore systems by Posadas et.al [28]. Fractal theory is based on the idea of "measurement at scale ε." For each ε, we quantify a system by ignoring irregularities of size less than ε, and monitor how these systems change as $\varepsilon \to 0$. In the case of fractals, the relationship between the measurements $N(\varepsilon)$ and the scale ε must obey power-law form:

$$N(\varepsilon) \sim \varepsilon^{-D} \qquad (3.1)$$

where D is a fractal dimension. This equation governs the structural distributions of many objects in nature. The box-counting dimension, one of the methods used to measure the fractal dimension of the two-dimensional object finds the "ε cover" of the object or the number of boxes of length ε needed to capture the object[38]. Practically, the object is overlaid by a regular grid of pixels of length L and number of pixels capturing the object is counted. This procedure is repeated using different values of L. Once the L becomes sufficiently small, $N(L)$ becomes equal to the number of points in the set and the limit above this is given by

$$D_b = \lim_{L \to 0} \frac{log\ N(L)}{log(\frac{1}{L})} \qquad (3.2)$$

24

where L is the size of the box, $N(L)$ denotes the number of boxes occupied by the object and D_b is the box-fractal dimension determined by Eq. [3.2]. D_b is estimated from the slope of the linear trend of the log-log plot of $N(L)$ versus L. One disadvantage of fractal method is that it does not consider the amount of mass inside the box $N_i(L)$ and hence, not able to resolve local densities of mass. A measure is multifractal if different fractal dimension exists on different parts of the support. The multifractal approach, when compared to the fractal framework, helps to determine the overall complexity present in the given dataset and thus, can be fully quantified. The method considers inner variation in a system by resolving local densities (e.g. pixel value 0-255 in the case of an image) and quantifies them in the shapes of the Multifractal spectrum. Multifractal techniques have been used in soil science to characterize soil pore systems [33].

$$P_i(L) = \frac{N_i(L)}{N_T} \tag{3.3}$$

where $P_i(L)$ is the mass probability in the ith box, $N_i(L)$ is the number of pixels containing mass in the ith box, and N_T is the total mass of the system. Eq. [3.3] is a way of quantifying local densities by evaluating the mass probability in the boxes. Illustration of spatial patterns of P_i ($L = 10$), and P_i ($L = 50$) for image of PSU Lion Shrine displayed in Figure 3.1:3. (L is expressed in pixels).

Figure 3.1:3 PSU Lion Shrine image with different multifractal scales, (a) original image of PSU Lion Shrine (2448 x 2448 x 3 pixels), spatial patterns of probabilities using varying pixel size (b) L = 25 pixels, and (c) L = 50 pixels[39]

The Multifractal theory describes the statistical properties of the fractal set in their singularity spectrum. Using Eq. [3.3], the singularity strength exponent α_i can be defined by

$$P_i(L) \sim L^{\alpha_i} \tag{3.4}$$

The number $\alpha_i = \dfrac{\log P_i(L)}{\log(L)}$ is also known as the Holder exponent, and represents

singularity strength of the ith box. This exponent denotes mass index of the concentration

of singular measure; the greater α_i is, smaller the concentration of the measure, and vice

versa [25]. For every box size L, the number of boxes of $N_\alpha(L)$ in which Holder exponent

α_i has a value within the range $[\alpha, \alpha + d\alpha]$ is found to scale as [40][41]:

$$N_\alpha(L) \sim L^{-f(\alpha)} \qquad (3.5)$$

where $f(\alpha)$ can be defined as fractal dimension of the set of boxes with singularity strength

α. Eq. [3.5] generalizes Eq. [3.1] by considering a range of indices to quantify the scaling

of the system.

An alternative measure of characterizing multifractal measures is possible through

scaling of the qth exponents of the singular measures [40][42]. If we capture the support of

the measure with boxes of size L and define $P_i(L)$ to be the probability measure in the ith

box, then a series of exponents parameterized by q can be defined as

$$\sum_{i=1}^{N(L)} P_i^q(L) = L^{(q-1)D_q} \qquad (3.6)$$

where D_q is the observed fractal dimensions defined from Eq. [3.6]. Limiting the size of

the box leading to zero gives the dimension definition as:

$$D_q = \lim_{L \to 0} \frac{1}{q-1} \frac{\log \sum_{i=1}^{N(L)} P_i^q(L)}{\log L} \qquad (3.7)$$

The exponent in Eq. [3.6] is called as the mass exponent of the qth order moment, $\tau(q)$

[42]:

$$\tau(q) = (q-1)D_q \qquad (3.8)$$

The generalized dimensions are exponents that characterize the non-uniformity of the measure; $q > 0$ features the crowded regions and $q < 0$ features the scarce ones [43]. In the range of values of q, certain values represent the dimension of a peculiar set, which supports a part of the measure. From the Eq. [3.7], boxes with a weight of unity, makes the fractal dimension D_q into capacity dimension, D_0. Same probability in all boxes in the system i.e. $P_i = 1/N$, makes $D_q = D_0$ for all values of q and hence, $\tau(q)$ becomes a linear function of q (homogenous fractal system).

The Legendre transformation connects the singularity spectrum $f(\alpha)$ and the mass exponent function $\tau(q)$ [44]

$$\alpha(q) = \frac{d\tau(q)}{dq} \tag{3.9}$$

And

$$f[\alpha(q)] = q\alpha(q) - \tau(q) \tag{3.10}$$

The multifractal spectrum $f(\alpha)$-spectra contains the same information as both equations of Eq. [3.9] and [3.10]. The Function $f(\alpha)$ is a concave shaped with a maximum at D_0. An easy method for the calculation of $f(q)$ and $\alpha(q)$ was provided by Chhabra and Jensen through Equations (3.12) and (3.13) [40]. Equation (3.11) represents a family of normalized measures $\mu_i(q, L)$ developed for values of $q > 0$ and $q < 0$ over ranges in steps of 0.1. $P_i(L)$ is the probability of measure captured in each ith box size L.

$$\mu_i(q, L) = \frac{P_i^q(L)}{\sum_{i=1}^{N(L)} P_i^q(L)} \tag{3.11}$$

$$f(q) = \lim_{L \to 0} \frac{\sum_{i=1}^{N(L)} \mu_i(q,L)\log[\mu_i(q,L)]}{\log L} \qquad (3.12)$$

And

$$\alpha(q) = \lim_{L \to 0} \frac{\sum_{i=1}^{N(L)} \mu_i(q,L)\log[P_i(q,L)]}{\log L} \qquad (3.13)$$

Eq. [3.12] and [3.13] provides the value of *f(q)* and *α(q)* for each q through the slopes of numerator against box size *L*. The curvature obtained through the functions *f(q)* and *α(q)* over a given *Δq* is the *f(α)*-spectra quantifying multifractal properties of the system. The Multifractal spectrum provides the information on the extreme regions of the measure i.e. where the measure is sparser or denser. Figure 3.1:4 shows the multifractal parameters of the *f(α)*-spectra.
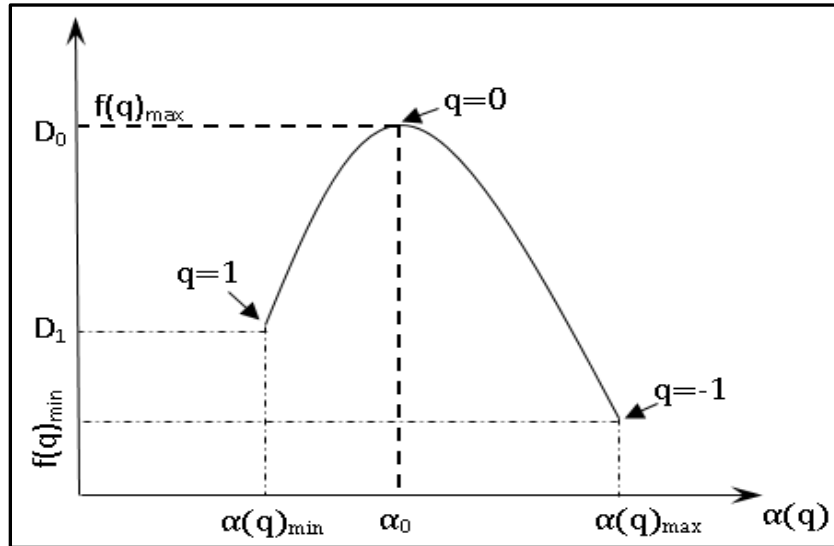
Figure 3.1:4 Multifractal spectrum features and parameters

3.1.3   Multifractal Analysis of Additive Manufacturing Images

Classical defects of pores, balling, cracks, etc. have different shapes, sizes and spatial arrangement on the layers of additive manufacturing processes. This defect is induced due to the variation of different parameters involved, and hence detection of this defects are important. Once detected these defects could help in understanding the additive manufacturing process and its variables. The symmetry and the curvature of the $f(\alpha)$-spectra provide information on the diversity of a system captured by images and defined by the diversity of scaling components q used to characterize it. Feature values to the left and right of D_0 represent positive and negative q values. Moments $q > 0$ amplify the contribution of boxes with the higher value pixels from mean (value towards 255 or white pixels) to the estimates of either $f(q)$ or $\alpha(q)$[28]. Similarly, $q < 0$ amplify the contribution of boxes with lower value pixels from the mean (value towards 0 or black pixels). In the Y-axis of $f(q)$, a magnitude of difference between D_0 and values of $f(1)$ or D_1 and $f(-1)$ represent the deviation of the system from normal behavior. In the x-axis of $\alpha(q)$, the difference $(\alpha_{max} - \alpha_{min})$ is used as a sign of heterogeneity in the system. Figure 3.1:5 (b) shows $f(\alpha)$-spectra of images with defects from chapter 1. The $f(\alpha)$-spectra among images shows the distinctively different shape and symmetry. The smallest heterogeneity is evident in the image with the crack defect and largest in the image with irregular pores. The right-hand side of the $f(\alpha)$-spectra in the image with irregular pore defect exhibits the largest difference in $D_0 - f(-1)$ and α value due to a presence of massive pore structure and overall heterogeneity in the image.
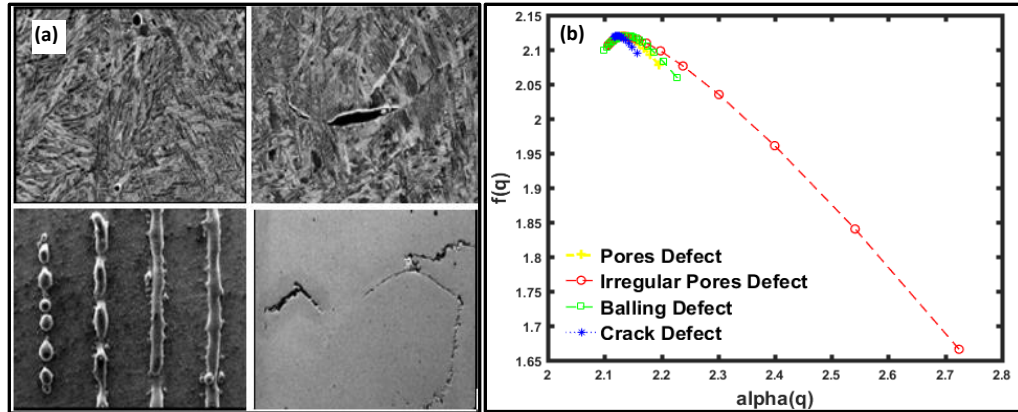
Figure 3.1:5 (a) Defect images of pores, irregular pores, balling and crack defect (b) $f(\alpha)$-spectra of images with defects

3.2 Uncorrelated Multilinear Principal Component Approach

Image processing is one of the widely growing areas in computer vision applications. With the rise in huge amount of image data, digital image processing is expanding rapidly and it is used to extract various features from the images. Many computer algorithm can do this without any human intervention. Digital images can prove useful in identifying and classifying various defects in images. Recently, there has been an increased in the use of sensor technology for process monitoring and fault diagnosis. The output of the sensor data is usually represented by spatial or time ordered data known as "profiles." In the past, most cases of manufacturing processes were characterized by single profiles. With development of sophisticated sensors, online sensing system can record more than one profile at each operation cycle. For example, Paynabar and Jin used "profiles" of ram force signals to process valve seats into engine heads in an engine head assembly process [45]. Strain gauge sensors were installed on each four uprights of a forging press, where each sensor recorded the tonnage force profile in every stamping operation. Colosimo et al. include the roundness of profile of a machined part at different sampling angles in a lathe-turning

process[46]. Since such multiple profiles are recorded through different sensor channels, they are called "multichannel profiles".

3.2.1 Tensor methodology for Images

Input data sets from many process monitoring processes are multi-dimensional in nature and can be defined using tensors. A number of indices are used to define the "order" of a tensor, with each index defined as one "mode". Gray-scale images are represented as a second-order tensor with column and row modes whereas video sequences are represented as third-order tensors with column, row and time modes. Often this type of high-order tensors suffers from the so-called curse of dimensionality in pattern recognition methods. Dimensionality reduction of subspace learning approach is regularly used to transform a multi-dimensional data set into low-dimensional feature space while retaining the most of the hidden structure. A standard method of principal component analysis is used for dimensional reduction but needs reshaping of tensor data into the form of 2-dimensional matrix. Recently, various methods were proposed to extensions of PCA operating directly on tensor objects.

3.2.2 Theory of UMPCA

Vectorized- PCA (VPCA) uses high-dimensional vector by stacking multi-channel profiles into one higher order vector but computational complexity and memory demands of VPCA are higher than PCA. Lu et al. introduced multi-linear PCA (MPCA) as an alternative to VPCA [47]. This method operates directly on the multi-dimensional data rather than vectorized version. This makes MPCA applicable to the higher order matrix or higher order tensor representation. MPCA provides principal component features with correlation as against regular PCA. Uncorrelated features are needed to ensure linear

independence with minimum redundancy in the features which are necessary for most pattern recognition tasks. Lu et al. proposed uncorrelated multilinear principal component analysis (UMPCA) to overcome the issue of correlation [48]. In UMPCA, several elementary multilinear projections (EMP) are solved with an objective to maximize the captured variance with constraint of zero-correlation. UMPCA is proving useful in many image processing and computer visions applications[49].

This section introduces the UMPCA methodology for unsupervised subspace learning of tensor objects. The major motivation of the work is developed through work of Lu et. al and Liu et. Al [48][50]. The methodology is to resolve the maximum number of uncorrelated features that can be extracted from multi-dimensional matrix or tensors by tensor to vector projection. In principal component analysis, the variance of the principal components is considered one at a time, starting from the first principal components that targets to capture the most variance and then second principal component and so on. The TVP consists of multiple elementary projections (EMP), which project a tensor $D \: \varepsilon \: R^{I}{}_{1}{}^{x...x}$ $^{I}{}_{N}$ to a scalar x through the N projection vectors as

$$x = D \: \mathrm{x}_1 \: \boldsymbol{u}^{(1)} \: \mathrm{x}_2 \: \boldsymbol{u}^{(2)} \: ... \: \mathrm{x}_N \: \boldsymbol{u}^{(N)} \qquad (3.14)$$

where $\boldsymbol{u}^{(n)}$ is the nth projection vector, x_n is the nth-mode multiplication. To calculate the nth-mode multiplication, the order-N tensor needs reshaping into matrices. The nth-mode multiplication x_n of tensor D and matrix M is defined as $D \: \mathrm{x}_1 \: M = MD_{(n)}$, where $D_{(n)}$ is the "flatting" of tensor data along the nth dimension. Figure 3.2:1 exhibits the EMP of an order-2 tensor to a scalar $x = D \: \mathrm{x}_1 \: \boldsymbol{u}^{(1)} \: \mathrm{x}_2 \: \boldsymbol{u}^{(2)}$. First, the order-2 tensor data $D \: \varepsilon \: R^{a \: x \: b}$ is flatted along the first dimension and then multiplied by the 1st projection vector $\boldsymbol{u}^{(1)}$, resulting in

a vector $D \times_1 u^{(1)} = u^{(1)} D_{(1)}$. Second, this vector of size 1 x b is then multiplied by the 2nd

projection vector $u^{(2)}$ to get the scalar $x = D \times_1 u^{(1)} \times_2 u^{(2)}$.
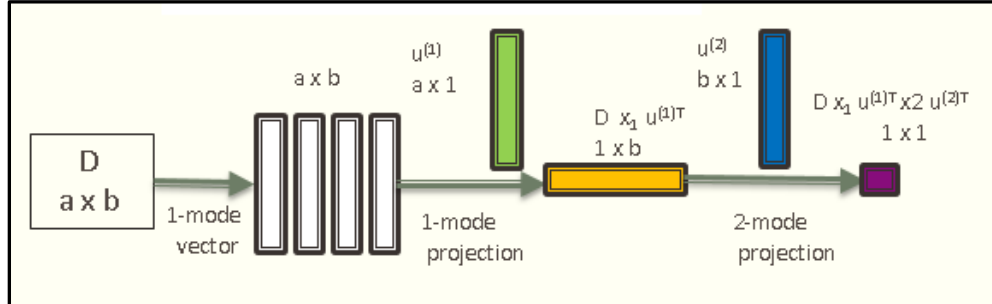
Figure 3.2:1 Elementary multilinear projection (EMP) of the order-2 tensor data[51]

The use of P EMPs will project the tensor data D to a vector $\mathbf{x} \in R^P$ as

$$x = D \; \text{x}_{n=1}^{N} \; \{u_p^{(n)}, n = 1,2, \dots, N\}_{p=1}^{P} \dots\dots\dots\dots\dots\dots\dots\dots\dots\dots\dots\dots\dots\dots(3.15)$$

where p denotes the index of EMP. For our stacked images data, we need the projection of

order-3 tensor χ to a 2-dimensional matrix Y. Then $x_m(p)$ is the projection of the mth image

χ_m by EMPs: $x_m(p) = \chi_m \; x_{n=1}^{N} \; \{u_p^{(n)}, n = 1,2, \dots, N\}$. As shown in Figure 3.2:2, g_p denotes

the pth coordinate vector and $g_p(m) = x_m(p)$. In order to maximize the variance of

projections and extract uncorrelated features, a constraint function will be imposed on the

p^{th} EMP.

Multilinear subspace learning produces a low-dimensional set of uncorrelated features. To

solve the constrained objective function, a sequential variance maximization algorithm is

utilized as shown in Figure 3.2:2. The P EMPs $\{u_p^{(n)}, n = 1,2, \dots, N\}_{p=1}^{P}$ are sequentially

estimated in P steps subject to the orthogonal and normalization constraints. Multilinear

subspace learning will transform the tensor data of size *a x b x M* into a matrix of uncorrelated features of size *p x M*.

Initialization:

$\boldsymbol{D_m} \; \varepsilon \; R^{I_1 \times \dots I_N}$, *m = 1, 2,.. , M*   → *A set of tensor examples*

P   → *desired feature vector length*

For *p = 1: P*

$g_p(m) = \boldsymbol{D_m} \; \mathrm{x}_{n=1}^{N} \; \{ \boldsymbol{u_p^{(n)^T}}, \mathrm{n} \; = \; 1,2, \dots, N\}$ → calculate the coordinate vector

If *p =1*

   Maximizing Var $(\boldsymbol{g_1})$ → *maximizing variance*

   Else

   Maximizing Var $(\boldsymbol{g_p})$ → *maximizing variance*

   Subject to $g_P^T g_q \; = 0, q = 1,2 \dots, p-1$ → *subject to the constraints*

End

   End
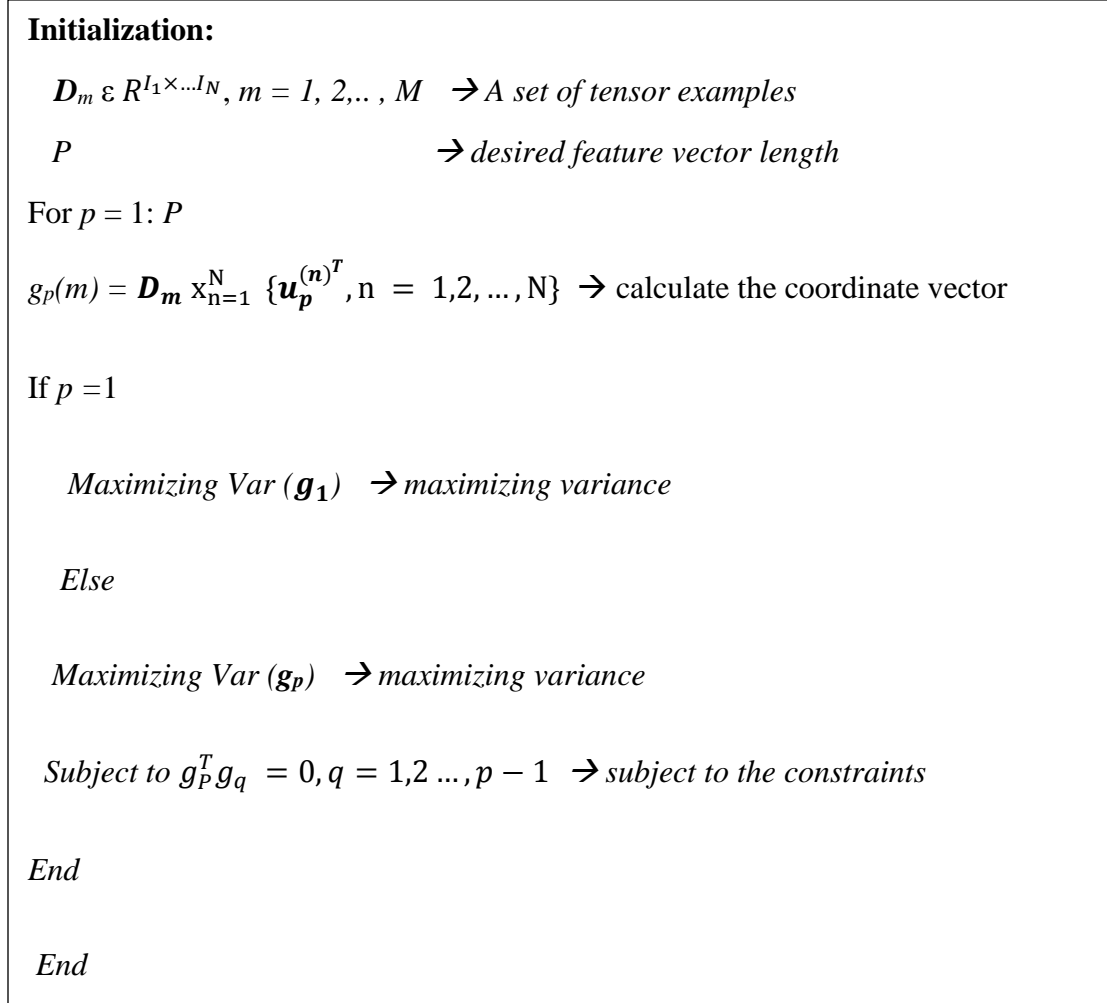
Figure 3.2:2 The sequential variance maximization algorithm for tensor decomposition

3.3   Parametric feature Analysis

Once we extract the features from the images of defects and control, we will use KS statistics to show a significant difference in value features from the group of defect induced image and control images [51][52]. Let $F_i(x)$ and $F_j(x)$ denotes the cumulative distribution

of the images in i^{th} and j^{th} group of no defect and defect induced respectively, then hypotheses of the KS test are:

$$H_0 : F_i(x) = F_j(x) \ \text{ or } \ H_0 : F_i(x) \neq F_j(x) \tag{3.16}$$

The KS test statistics is tested against the corresponding cut-off value given by $c_\alpha \sqrt{\frac{n_1 + n_2}{n_1 n_2}}$, where n_1 and n_2 are the number of independent observations in group of no defect images and defect induced images, the significant level of α-value is 0.05 and c_α is roughly calculated as 1.36. If the KS test statistic is greater than the cut-off value, the null hypothesis H_0 will be rejected and the cumulative distribution functions of two groups are claimed to be different at significant level of 0.05 as exhibited in Figure 3.3:1. Thus, higher the magnitude on KS statistics, the more significant the feature is. We will test the statistical significance for eleven multifractal parameters for multifractal analysis and ten features of UMPCA analysis.
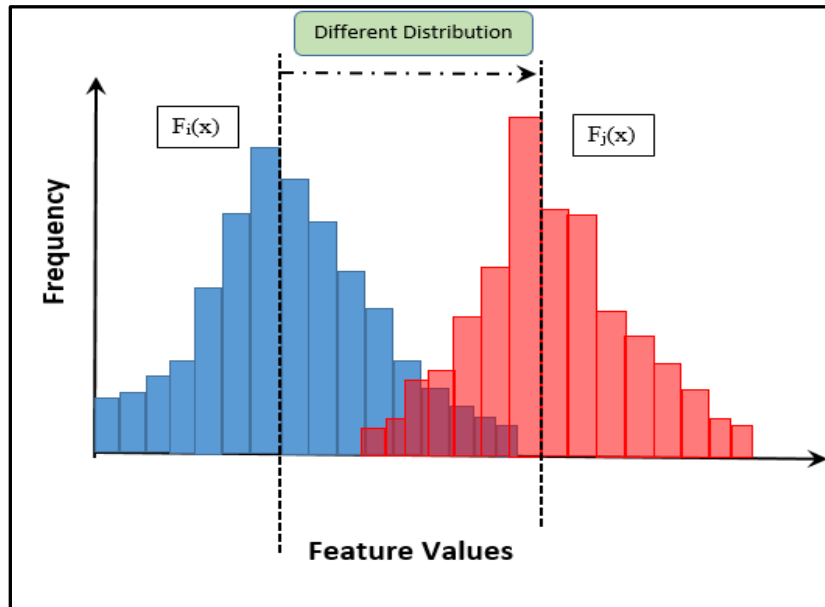
Figure 3.3:1 Illustration of the Kolmogorov–Smirnov statistic

CHAPTER 4. CHARACTERIZATION AND MODELING

OF BUILD DEFECTS

4.1   4.1 Introduction

This chapter details the design of experiments, experimental set-up and simulation of defects on AM images for process modeling and characterization of build defects

4.1.1   4.2 Design of Experiments

In our research, we propose novel methods of multifractal analysis and UMPCA to study the in-process images of additive manufacturing for process-machine modeling and defect characterization. Figure 4.1:1 summarizes the design of experiment used in this study.
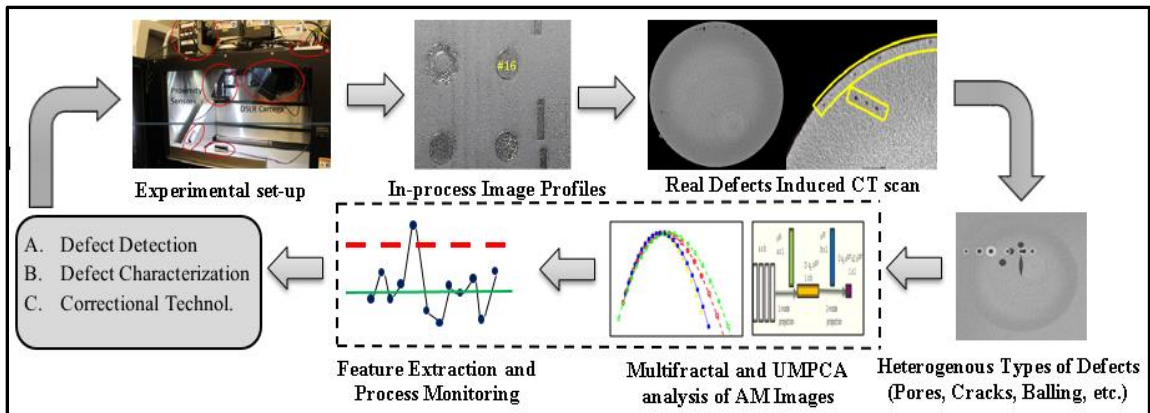
Figure 4.1:1 Design and Methodology of the research

4.1.2   4.2.1 Experimental Set-up

In our research, we used the data from the AmericaMakes project carried out at the Applied Research Laboratory at Penn State. A powder-based additive manufacturing process was planned and executed under a controlled environment. The additive manufacturing technique used in the process is a direct metal laser sintering process. The

DMLS process allows for complex geometries to be built directly from a 3D CAD model without any tooling. The entire manufacturing operation has been carried out inside the EOS M 280 Laser Sintering System for DMLS. The camera housing and fixture designs were completed and built using the Stratasys Fortus 400. Designs allowed for mounting within the EOS M280 build chamber, with electronics. Parts were coated with an epoxy layer to prevent outgassing from the high-vacuum environment. Proximity sensors were used to sense the motion of the re-coater arm to trigger image acquisition at the appropriate time in a non-invasive manner. Figure 4.1:2 shows the several images of the set-up.
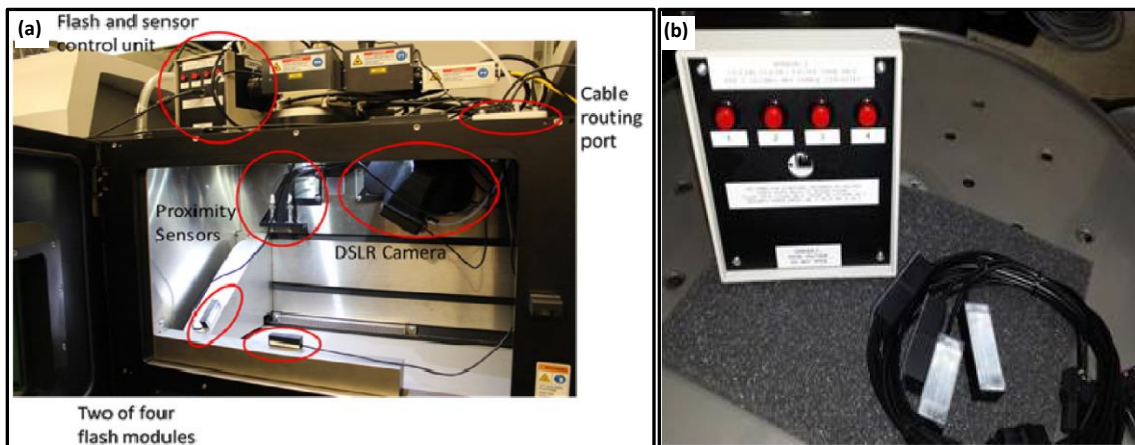
Figure 4.1:2 (a) Experimental setup inside the EOS M280, (b) electronics to operate the flashes and proximity sensors

The test plan of the experiment was to generate intentional defects in the components in the number of ways. The defects were developed by varying process parameters (laser power, scan velocity), by building geometries that exhibit extreme distortion during the build with variety of "supports" applied (e.g. no support, weak support, etc.) and by building components near the corners of the build plate, where defects caused by scanning inaccuracies have been observed. Images were acquired at each layer using a variety of flash locations, both immediately after recoating of powder layers and immediately after scanning. Figure 4.1:3 (a) shows the in-process images of the manufacturing bed from the

experiment from different image sensors. The components build at the end of the additive

manufacturing process, and the individual variation in parameters for the selected

components can be seen in Figure 4.1:3 (b).
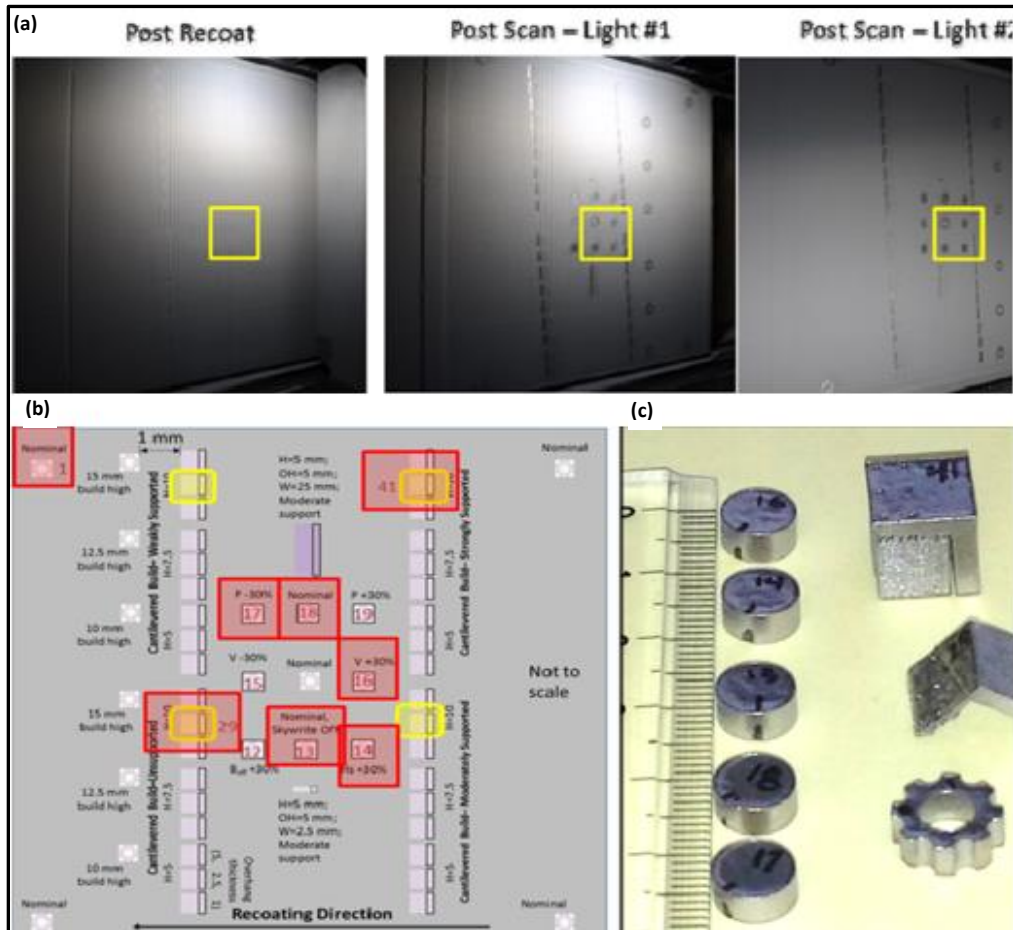
Figure 4.1:3 (a) In-situ images of machine after recoating and after laser scanning, (b) test plan for variation of parameters, and (c) component build by AM

4.1.3　3D Computerized Tomography

From the experiment, a subset of components having a high likelihood of defects was

selected for 3D digital computerized tomography scan analysis. The 3D CT scan is useful

for detecting the inter build defects between the layers of the components. The 3D CT scan

revealed clear evidence of internal defects. An example from the experiment "Sample No.

16 with the scan velocity of +30%" is shown in Figure 4.1:4. Similarly, other components were induced with intentional defects with variation in other parameters.
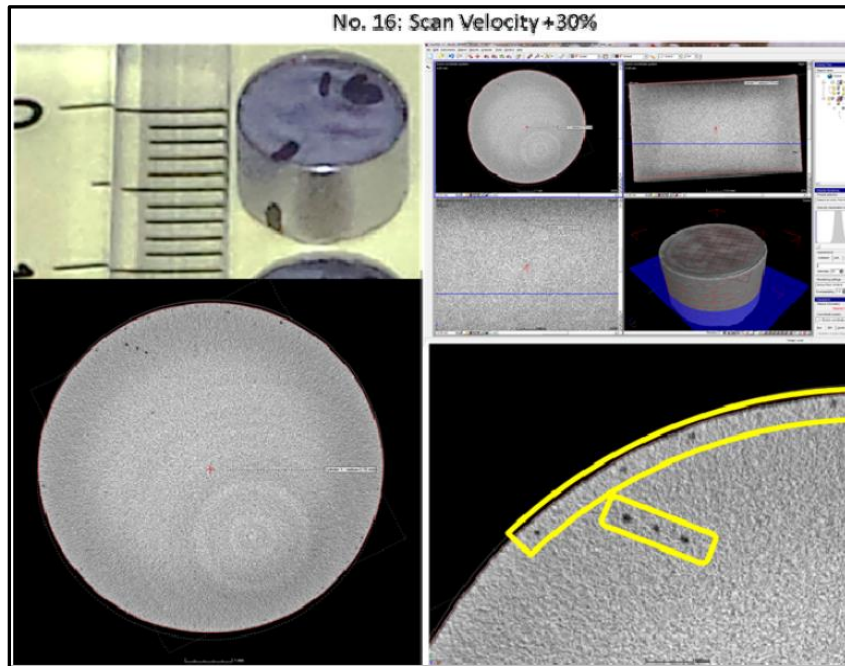
Figure 4.1:4 Computerized tomography of components exhibiting induced defects

4.2 Transformation of 3D scan images into 2D profiles

For our research, we have used the 3D CT scan data of the component and processed them in the software Volume Graphic myVGL 3.0 to extract the 2D profiles of the surface images of the components. Images were generated through slicing of the component file from the top view, and each image has a circular profile with a black background. Actual images are a grayscale image with the size of 817 X 812 pixels, with a pixel size of 178.7 µm. Once the 3D scan components were transformed into 2D image profiles, images with visible defects and images without visible defects were separated into two groups. Images from both groups can be seen in Figure 4.2:1 (b) and (c). Processed images from the group of defects, contained defects of varying size and shape and randomly distributed throughout

the surface. The noise in the background of the images was neutralize using bootstrapping method.
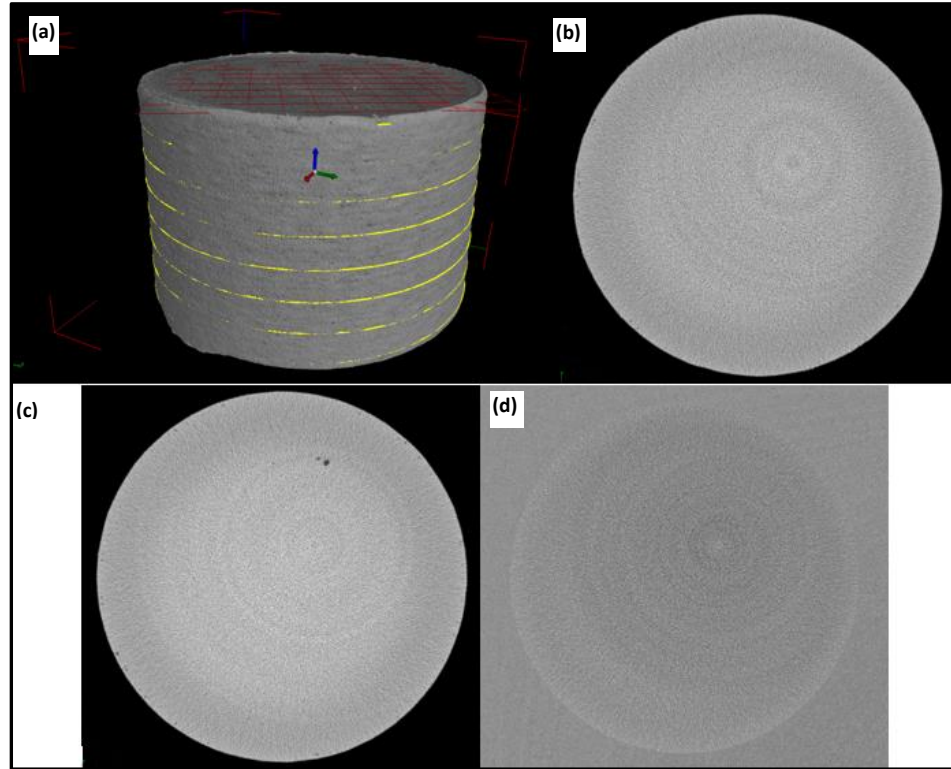
Figure 4.2:1 (a) 3D CT scan of the AM build component, (b) top view of 2D layer without defect, (c) top view of 2D layer with induced defect, and (d) background neutralize by bootstrapping method

4.3   Simulation of Heterogenous Defects

Once the images of interest were developed, the process of simulation of different types of defect took place. We used software Matlab R2016a for the simulation of various defects on the images. We previously mentioned the different types of defect and their shapes found in AM processes in Chapter 2 and with the characteristics of real defect induced images, we developed the classical defects discovered in the AM processes on the images free from defects. We used 120 images for our experiment in which 60 images were control images without any defect and 60 images with simulated defects. The defect sizes were

41

increased over the images by one pixel every time. Images from 60 to 80 were simulated with circular pore defects and thereby increasing the pore defect radius by a pixel every time. Similarly, images from 80 to 100 were simulated with a crack in which the minor axis was increased by a pixel every time. Images from 100 to 120 were simulated which balling defect, a defect with highest variation in pixel values in all defects (0-255) Hence, the balling defects were simulated with both black and white pixels. We used software Matlab R2016a for the simulation of defects on the images. The stream of images with all the defects induced can be seen in Figure 4.3:1.
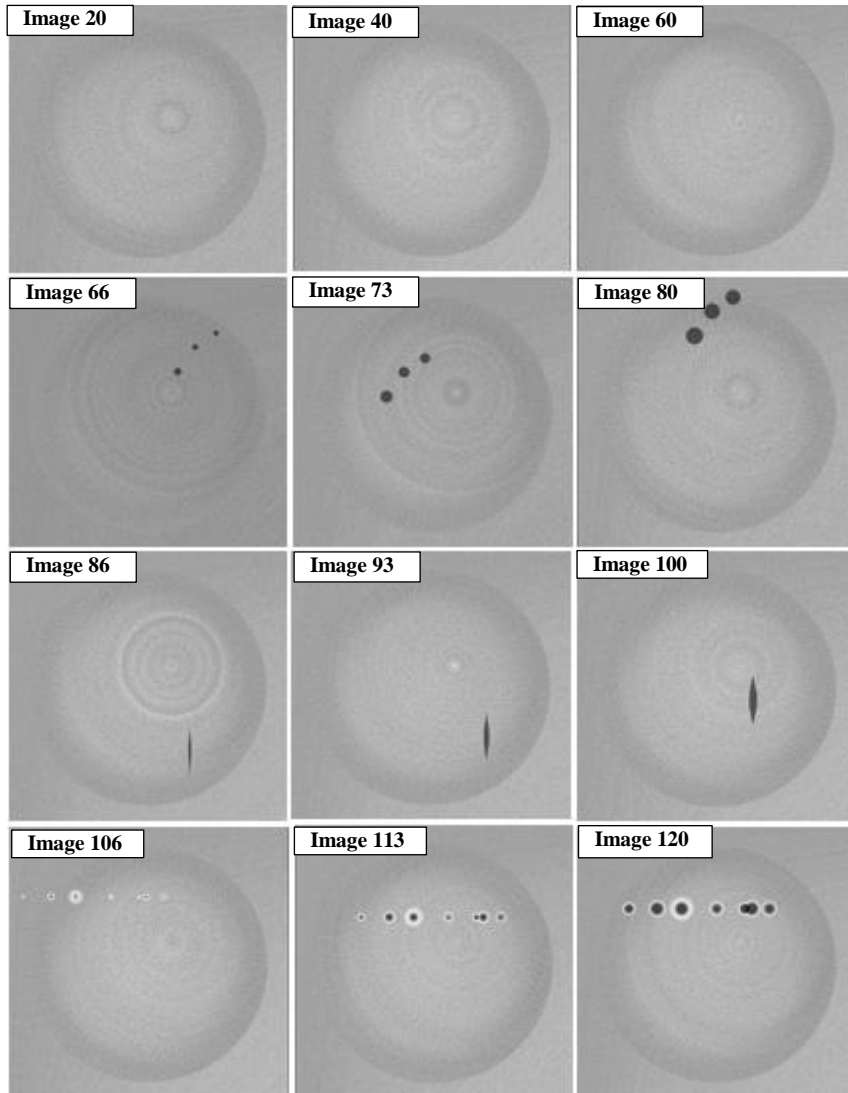
Figure 4.3:1 In-situ stream of 120 images with control (1-60) and pore defect, crack defect and balling defect (61-120)

4.4 Summarization of Data

Post simulation operation, we have successfully grouped the images into two groups of control (Images 1-60) and defects (Images 61-120). These 120 images are a representation of in-situ process modeling of the additive manufacturing process. Our approach of multifractal analysis and UMPCA will use these images as input data and will give us output in the form of parametric features correlating to the heterogeneity or variation

43

induced in the images. We use parametric features from both the groups and perform parametric analysis to find out if our approach is significant to differentiate the parameters relating to two groups of control and defects. Also, we compare results from both methods and deduce which approach is significantly better for the process monitoring and fault diagnostics in additive manufacturing.

CHAPTER 5.   RESULTS AND CONCLUSIONS

5.1   Introduction

This chapter outlines the results of the experiment, statistical analysis of parametric features and conclusion arising out of the investigation.

5.2   Multifractal Analysis of In-situ Images

The multifractal spectrum of images provides us with features quantifying the defect patterns and irregularities encountered in the images via the shape of the $f(\alpha)$-spectra. The 120 in-situ images were implemented through the multifractal program developed by Tegy J. Vadakkan in the Matlab Central 2009 [53]. The output from the multifractal code is displayed in the form of a graph in Figure 5.2:1 (b). Figure 5.2:1 (a) shows the four images from the in-situ stream of images used in the research depicting control and different defects of pores, cracks and balling. Corresponding multifractal $f(\alpha)$-spectra of the four images is shown in Figure 5.2:1 (b) in different colored markers for differentiation.
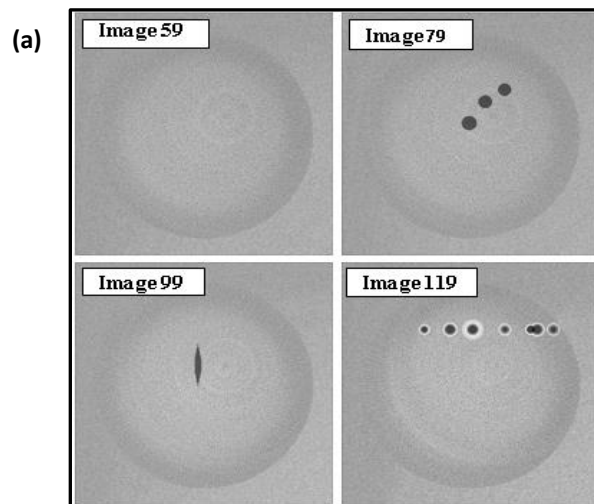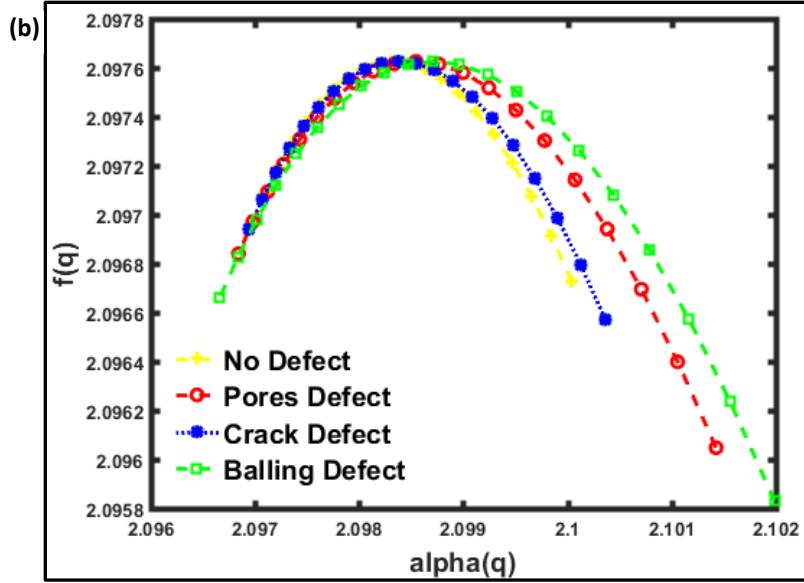
Figure 5.2:1 (a). Four in-situ images with no defect, pores defect, crack defect and balling defect (b) multifractal $f(\alpha)$-spectra of the four in-situ images

The multifractal method considers inner variation in an image system by resolving local densities (pixel value 0-255) and quantifies them in the shapes of the multifractal spectrum. The multifractal spectrum has quantified the differences in four in-situ images by considering different defects induced in them. In the $f(q)$-axis, a comparison is between D_0 and values of $f(1)$ or D_1 and $f(-1)$. In the $\alpha(q)$ axis, the difference ($\alpha_{max} - \alpha_{min}$) is used as an indication of the heterogeneity of a system. The lowest variation in heterogeneity is the image with control quality or no defects. The highest variation can be seen in balling defect due to highest deviation of pixels, size and shape of defect. We checked the statistical significance for eleven multifractal parameters with dominant features of $f(1)$ or D_1, $f(-1)$, $\alpha(-1)$, $\alpha(1)$ and $\alpha(-1)-\alpha(1)$, $f(-1)-f(1)$, $\alpha(-1)-\alpha(0)$, $\alpha(0)-\alpha(1)$, $f(0)-f(-1)$, $f(0)-f(1)$ and D_0. The KS test statistics is tested against the corresponding critical value of 0.25. From the Figure 5.2:2 (a), ten out of eleven features have KS statistics greater than 0.25. Moreover, all significant features have the KS statistics greater than 0.5. Figure 5.2:2 (b) shows the visualization of feature ($f_{max} - f_{min}$) of all the images in the form of a histogram. The values

of feature (f_{max}- f_{min}) from the group of no defect images are marked in blue, and the group of defect-based images marked in red. Both plots show distinct differences between the group of no defect and defect induced images. The group of images having defects have bigger mean and variation than the group of images with no defects. Figure 5.2:3 (a) and (b) show the visualization of significant feature (f_{max}- f_{min}) and (α_{max}- α_{min}) for all 120 images. Feature values from the group of defect induced images show distinct pattern different from the group of control images and significantly increase when the defect size and characteristics increases. It is an indication of the heterogeneity of a system. One feature with KS statistics below the cut-off value is the distribution of fractal dimension D_0. Unlike multifractals parameters, fractal dimension characterizes the average properties of images and cannot provide information on deviation from average behavior in the system.
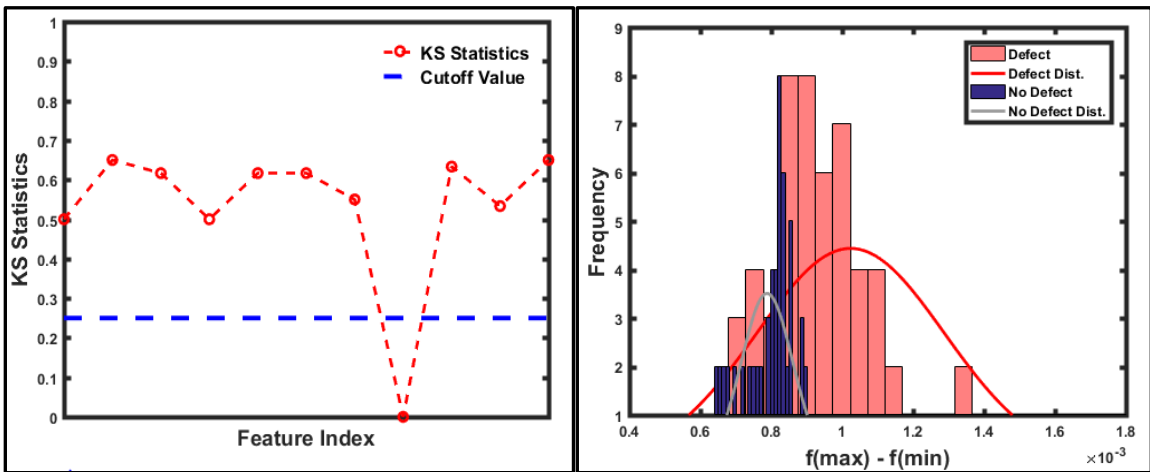
Figure 5.2:2 (a). KS statistics for multifractal parameters (b) The visualization of feature (f_{max}- f_{min}) in the form of histogram
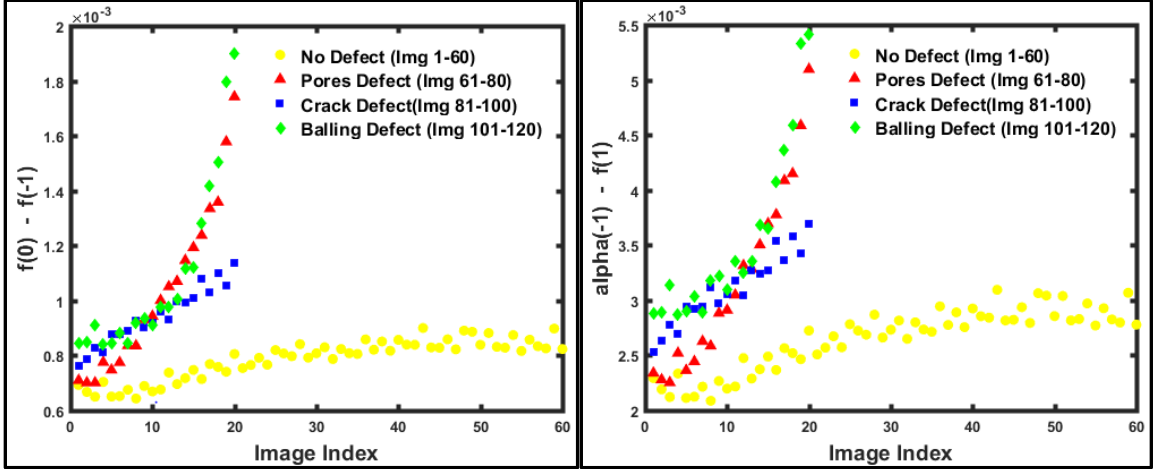
Figure 5.2:3 (a) The visualization of feature (f_{max}- f_{min}) for all images (b) The visualization of feature (α_{max}- α_{min}) for all images

5.3 UMPCA analysis of In-situ Images

Multilinear subspace learning transforms the tensor data of size *a x b x M* into a matrix of uncorrelated features of size *p x M* [51]. The 120 in-situ images form a multi-dimensional matrix data representing layer-wise acquired images of in process additive manufacturing operation. The input data for the UMPCA program will be tensor data of size 817 x 812 x 120 where the size of each image is 817 x 812. This tensor or multi-dimensional matrix data was implemented through the UMPCA algorithm presented in the paper of Uncorrelated Multilinear Principal Component Analysis for Unsupervised Multilinear Subspace Learning [39]. We extracted ten uncorrelated features from the UMPCA code, so our output data from the algorithm was a matrix of uncorrelated features of size 10 x 120. Figure 5.3:1 (a) and (b) shows the variance explained by the UMPCA and KS test statistics of 10 features tested against the corresponding critical value of 0.25 respectively.
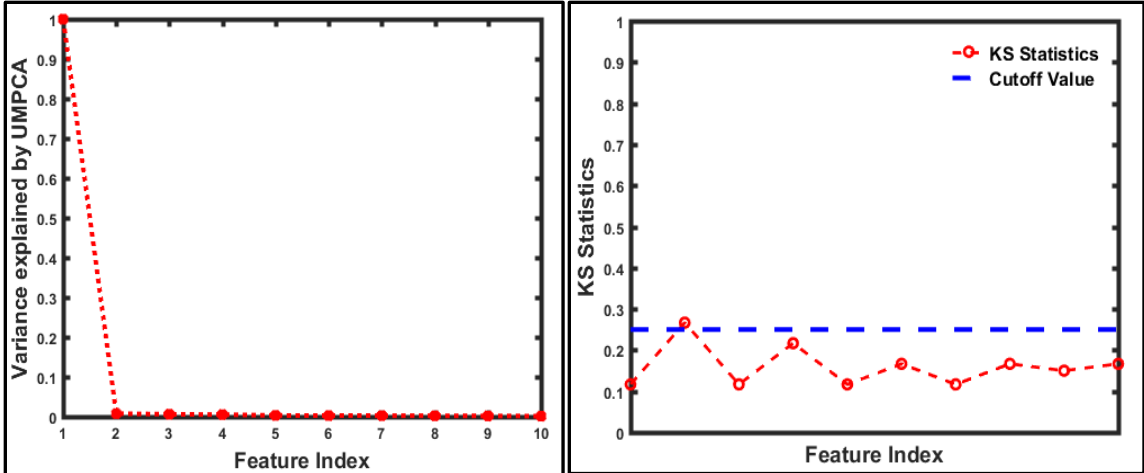
Figure 5.3:1 (a) Variance explained by the 10 UMPCA features, and (b) KS statistics for UMPCA features

Of all the features extracted, the first feature explains almost all the variance in the multidimensional matrix data of in-situ images shown in Figure 5.3:1(a). In all ten features, only second feature has KS statistics greater than cut off value but not far from it. Figure 5.3:2 shows the visualization of the lone significant feature in the form of histogram.
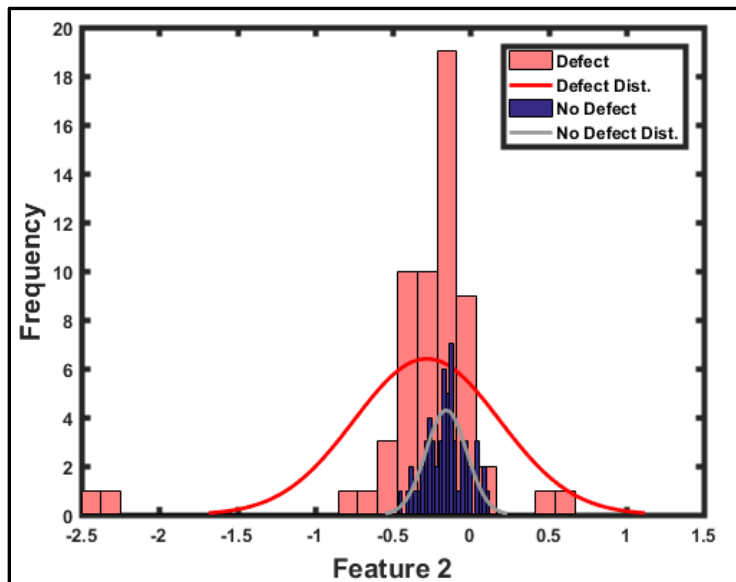
Figure 5.3:2 Visualization of significant feature extracted through UMPCA

5.4 Comparison of Multifractal and UMPCA results

In this research, we approach the subject of process modeling and defect characterization in additive manufacturing through multifractal and UMPCA approach. Given the results of both approach, the multifractal analysis clearly has an advantage in detecting the various defects induced in the AM processes. In the eleven features extracted from the multifractal spectrum of $f(\alpha)$-spectra, ten features were statistically significant in KS statistics test. In contrast, UMPCA approach only provided one significant feature in a total of ten features extracted from the tensor data when tested against KS statistics test. The parametric features of multifractal analysis easily distinguish the images of defects/discontinuities from the control ones. Feature values from the group of defect induced images show distinct pattern different from the group of control images and significantly increase as the defect size increases. The features correlating to the defects increases with the change in size, shape and spatial arrangement of defects and hence, provides unprecedented opportunity in process monitoring and defect detection in AM.

CHAPTER 6.   SUMMARY AND FUTURE WORK

6.1   Introduction

This chapter describes the summary, contributions of this research in sensor-based, in-situ process monitoring of additive manufacturing as well as the direction of future work in this area.

6.2   Summary of thesis research

Most of the previous work in additive manufacturing has been limited to defect/discontinuities detection, and very few considered the characterization of defects with respect to size, shape and spatial arrangement of defects. A wide range of defects are produced in AM processes and hence different methods of detection and characterization evolved separately considering defects. In this thesis research, we approached the shortcomings of additive manufacturing through image-guided methods of multifractal and UMPCA analysis.

6.2.1   Significance of Multifractal Analysis

Since the advent of fractal geometry, it has been used extensively to describe the complexity of non-linear systems such as ecology, signal and image processing, soil mechanics, etc.[25][27][28]. The compelling reasons for using fractal theory in many scientific fields are based on the concept that complex systems could be explained using a relatively low number of parameters. Compared to classical approaches of image analysis, fractal and multifractal analysis are advantageous in the way of handling of irregularities.

For our research, Multifractal analysis contributed in following ways:

- Multifractal analysis of images characterized the different defects induced in the AM without the need for any image processing technique.

- Multifractal approach considered the size, shape and spatial arrangement of the defects and fully extracted the irregularities and heterogeneity induced in the process.

- Multifractal $f(\alpha)$-spectra successfully separated the defect and no defect images based on the feature parameters.

- Ten out of eleven features used in the experiment have KS statistics greater than the critical value of 0.25, indicating significant differences between no defect and defect induced images. Moreover, all significant features have the KS statistics greater than 0.5.

- Feature values from the group of defect induced images show distinct pattern different from the group of control images and significantly increase as the defect size increases. This give room for sensitivity analysis in the future.

This shows that the approach presented works for any defect/irregularity induced in the process and provides effective parameters for in-situ fault detection. This methodology can help in solving the shortcomings of additive manufacturing and achieving goals of high quality and repeatability.

6.2.2 Limitations in UMPCA approach

Input data sets from many process monitoring processes are multi-dimensional in nature and can be formally represented using tensor. Uncorrelated Multilinear Principal

Component Analysis extracts the principal component features from the multi-dimensional image data or tensor that points to the irregularities in the images. Given the in-situ images of AM used in this research, UMPCA approach contributed in the following way and showed some limitation:

- UMPCA analysis of images characterized the different defects induced in the AM without the need of any image processing technique.

- UMPCA uses the sequential variance maximization algorithm to provide features that describes the variance in the image dataset.

- UMPCA could not successfully differentiate the group of images with defect from group images of control or no defects used in this research. UMPCA approach only provided one significant feature in total ten features extracted from the tensor data in KS statistics test. The lone significant feature value was not far from KS cut-off value.

- Feature values from the group of induced defect images did not show distinct differences from values for the group of control images.

This shows that UMPCA parametric features were not able resolve the variation in image characteristics induced through simulation of defects. This concludes that the UMPCA approach is not effective in catching the small deviation or heterogeneity in images produced due to defects and irregularities.

6.3   Research Contribution to Image-Guided Additive Manufacturing

Additive manufacturing solves many shortcomings that come with traditional processes, but AM has its own complications that need to be addressed for the successful development

of additive manufacturing technologies. In order to successfully monitor the quality control and fault diagnostics, this research develops and implements a multifractal approach which provide data quantifying some of the most important factors in additive manufacturing process. Specific contributions are as follows:

1. **Implementation of in-situ image-based methodology:** There are different types of sensors used in AM processes depending on the application, popular being photodiodes and digital cameras. We proposed a method of multifractal analysis of in-situ images of AM process acquired through image sensors that can help in real-time detection and characterization of defects. Proximity sensors were used in the experiment to sense the motion of the re-coater arm to trigger image acquisition at the appropriate time in a non-invasive manner.

2. **Correlation of process parameters to defects/discontinuities:** The multifractal analysis of images provided us with features quantifying the defect patterns and irregularities encountered in the images in shape of *f(α)*-spectra. It considered the size, shape and spatial arrangement of the defects. Statistical significance for eleven multifractal parameters from *f(α)*-spectra were analyzed against the KS statistics test. Ten out of eleven features used in the experiment had KS statistics greater than the critical value of 0.25.

3. **Classification of images in group of the faults and control:**

   The multifractal approach presented successfully differentiated the control and defect groups indicating that the defects/irregularity induced in the process were captured by the multifractal spectra. Feature values from the defect group show

distinct patterns from the group of control group and significantly increase in value as the defect characteristics of size, shape and pixel variation increases.

Through this research, we attempted to tackle one of the issues of defect and discontinuities in additive manufacturing. Multifractal analysis captures the inner variations in images by resolving local densities and expresses them in shapes of the multifractal spectrum. The parametric features provided by $f(\alpha)$-spectra successfully distinguishes the images of control and defects.

6.4   Future work in Image-guided Additive Manufacturing

Detection of the process failure is critical, and it would be beneficial to detect such failure in real-time so correctional technologies can be applied as soon as error and defect arise. This would require detection of the characteristics that correlates to the deviation in AM systems. For this purpose, in-situ technologies will have utmost importance in coming years and image sensors will suffice to meet this urgent need. Sensor methodologies need algorithms and methodologies that not only detect but also sufficiently characterizes the defects. Multifractal analysis can be one such method which successfully detects the smallest deviation in in-situ image characteristics. The next step in future work will be differentiating the characteristics of different defects and irregularities from each other. Different defects/discontinuities are related to change in different parameters and this work will bring higher sophistication and better understanding in dealing with irregularities in AM.

References

[1]   N. Serres, D. Tidu, S. Sankare, and F. Hlawka, *Environmental comparison of MESO-CLAD?? process and conventional machining implementing life cycle assessment*, vol. 19, no. 9–10. Elsevier Ltd, 2011.

[2]   T. Wohlers, "Making Products By Using Additive Manufacturing," *Manuf. Eng.*, vol. 146, no. 4, pp. 70–74,76–77, 2011.

[3]   "GE   Brilliant   Factory."   [Online].   Available: https://www.ge.com/stories/brilliantfactory. [Accessed: 10-Apr-2017].

[4]   ASTM F42.91, "F2792-12a: Standard Terminology for Additive Manufacturing Technologies," *ASTM International*, 2012. [Online]. Available: http://www.astm.org.

[5]   E. W. R. and A. R. Nassar, "A survey of sensing and control systems for machine and process monitoring of directed-energy metal-based additive manufacturing," *Rapid Prototyp. J.*, vol. 21, no. 2, pp. 159–167, 2015.

[6]   H. Attar, M. Calin, L. C. Zhang, S. Scudino, and J. Eckert, "Manufacture by selective laser melting and mechanical behavior of commercially pure titanium," *Mater. Sci. Eng. A*, vol. 593, pp. 170–177, 2014.

[7]   P. Edwards, A. O'Conner, and M. Ramulu, "Electron Beam Additive Manufacturing of Titanium Components: Properties and Performance," *J. Manuf. Sci. Eng.*, vol. 135, no. 6, p. 061016, 2013.

[8]   S. Tammas-Williams, H. Zhao, F. Léonard, F. Derguti, I. Todd, and P. B. Prangnell, "XCT analysis of the influence of melt strategies on defect population in Ti-6Al-4V components manufactured by Selective Electron Beam Melting," *Mater. Charact.*, vol. 102, pp. 47–61, 2015.

[9]   R. Li, J. Liu, Y. Shi, L. Wang, and W. Jiang, "Balling behavior of stainless steel and nickel powder during selective laser melting process," *Int. J. Adv. Manuf. Technol.*, vol. 59, no. 9–12, pp. 1025–1035, 2012.

[10]   H. J. Niu and I. T. H. Chang, "Instability of scan tracks of selective laser sintering of high speed steel powder," *Scr. Mater.*, vol. 41, no. 11, pp. 1229–1234, 1999.

[11]   F. Wang, H. Mao, D. Zhang, X. Zhao, and Y. Shen, "Online study of cracks during laser cladding process based on acoustic emission technique and finite element analysis," *Appl. Surf. Sci.*, vol. 255, no. 5 PART 2, pp. 3267–3275, 2008.

[12]   S. Kleszczynski, J. Zur Jacobsmühlen, J. T. Sehrt, and G. Witt, "Error detection in laser beam melting systems by high resolution imaging," *23rd Annu. Int. Solid Free. Fabr. Symp.*, pp. 975–987, 2012.

[13]   M. Van Elsen, *Complexity of Selective Laser Melting: a new optimisation approach*. 2007.

[14]   J. P. Kruth, G. Levy, F. Klocke, and T. H. C. Childs, "Consolidation phenomena in laser and powder-bed based layered manufacturing," *CIRP Ann. - Manuf. Technol.*, vol. 56, no. 2, pp. 730–759, 2007.

[15] D. Gu and Y. Shen, "Balling phenomena in direct laser sintering of stainless steel powder: Metallurgical mechanisms and control methods," *Mater. Des.*, vol. 30, no. 8, pp. 2903–2910, 2009.

[16] T. H. C. Childs, C. Hauser, and M. Badrossamay, "Mapping and Modelling Single Scan Track Formation in Direct Metal Selective Laser Melting," *CIRP Ann. - Manuf. Technol.*, vol. 53, no. 1, pp. 191–194, 2004.

[17] G. Tapia and A. Elwany, "A Review on Process Monitoring and Control in Metal-Based Additive Manufacturing," *J. Manuf. Sci. Eng.*, vol. 136, no. 6, p. 060801, 2014.

[18] T. Craeghs, S. Clijsters, E. Yasa, and J.-P. Kruth, "Online quality control of selective laser melting," *Solid Free. Fabr. Proc.*, pp. 212–226, 2011.

[19] S. K. Everton, M. Hirsch, P. Stravroulakis, R. K. Leach, and A. T. Clare, "Review of in-situ process monitoring and in-situ metrology for metal additive manufacturing," *Mater. Des.*, vol. 95, pp. 431–445, 2016.

[20] S. Berumen, F. Bechmann, S. Lindner, J.-P. Kruth, and T. Craeghs, "Quality control of laser- and powder bed-based Additive Manufacturing (AM) technologies," *Phys. Procedia*, vol. 5, pp. 617–622, 2010.

[21] T. Furumoto, M. R. Alkahari, T. Ueda, M. S. A. Aziz, and A. Hosokawa, "Monitoring of Laser Consolidation Process of Metal Powder with High Speed

Video Camera," *Laser Assist. Net shape Eng. 7 (LANE 2012)*, vol. 39, no. 0, pp. 760–766, 2012.

[22] M. Pavlov, M. Doubenskaia, and I. Smurov, "Pyrometric analysis of thermal processes in SLM technology," *Phys. Procedia*, vol. 5, no. PART 2, pp. 523–531, 2010.

[23] M. Islam, T. Purtonen, H. Piili, A. Salminen, and O. Nyrhilä, "Temperature profile and imaging analysis of laser additive manufacturing of stainless steel," *Phys. Procedia*, vol. 41, pp. 835–842, 2013.

[24] E. Rodriguez, F. Medina, D. Espalin, C. Terrazas, D. Muse, C. Henry, and R. B. Wicker, "Integration of a thermal imaging feedback control system in electron beam melting," *WM Keck Cent. 3D Innov. Univ. Texas El Paso*, no. Figure 1, pp. 945–961, 2012.

[25] L. Seuront, *Fractals and multifractals in ecology and aquatic science*. 2010.

[26] B. B. Mandelbrot, "The fractal geometry of nature /Revised and enlarged edition/," *New York*, 1983.

[27] M. Vetierli, "~ velets and Signal," no. October, pp. 14–38, 1991.

[28] A. N. D. Posadas, D. Giménez, R. Quiroz, and R. Protz, "Multifractal Characterization of Soil Pore Systems," *Soil Sci. Soc. Am. J.*, vol. 67, no. 5, p. 1361, 2003.

[29] "Fractal leaves." [Online]. Available: https://s-media-cache-ak0.pinimg.com/736x/5c/8a/be/5c8abeb9f7f90e629e749737cb8247cb.jpg. [Accessed: 28-Mar-2017].

[30] "Fractal Cloud." [Online]. Available: https://d18l82el6cdm1i.cloudfront.net/image_optimizer/a011fe20bbe12017d518b269d9917e146a4c03d5.jpg. [Accessed: 28-Mar-2017].

[31] "Fractal peacock." [Online]. Available: http://www.philliplysyj.com/uploads/1/0/8/6/10863112/_9679260.jpg?377. [Accessed: 28-Mar-2017].

[32] "Apollo13.GIF (400×400)." [Online]. Available: http://users.math.yale.edu/public_html/People/frame/Fractals/Panorama/Art/Hollywood/Apollo13.GIF. [Accessed: 28-Mar-2017].

[33] "Kandariya-Mahadev_Temple.jpg (500×500)." [Online]. Available: http://dataisnature.com/images/Kandariya-Mahadev_Temple.jpg. [Accessed: 28-Mar-2017].

[34] "Fractal Chinese Structure." [Online]. Available: https://s-media-cache-ak0.pinimg.com/236x/fa/00/6b/fa006b95f97ab6fef20d1c51881dbd3b.jpg. [Accessed: 28-Mar-2017].

[35] B. B. Mandelbrot, *The Fractal Geometry of Nature*, vol. 51, no. 3. 1983.

[36] S. R. T. Kumara and S. T. S. Bukkapatnam, *Characterization and Monitoring of Nonlinear Dynamics and Chaos in Manufacturing Enterprise Systems*, no. October. 2007.

[37] H. Yang and E. Lee, *Characterization and Monitoring of Nonlinear Dynamics and Chaos in Complex Physiological Systems, in Healthcare Analytics: From Data to Knowledge to Healthcare Improvement*, Doi: 10.10. Hoboken, NJ, USA: John Wiley & Sons, Inc, 2016.

[38] R. F. Voss, "Fractals in nature: from characterization to simulation," *Sci. fractal images*, pp. 21–70, 1988.

[39] "PSU Lion Shrine (2448×2448)." [Online]. Available: http://sites.psu.edu/arorakaran28/wp-content/uploads/sites/19445/2014/10/image5.jpg. [Accessed: 28-Mar-2017].

[40] A. B. Chhabra, C. Meneveau, R. V. Jensen, and K. R. Sreenivasan, "Direct determination of the f_alpha singularity spectrum," *Phys. Rev. Lett.*, vol. 62, no. 9, pp. 5284–5294, 1989.

[41] T. C. Halsey, M. H. Jensen, L. P. Kadanoff, I. Procaccia, and B. I. Shraiman, "Fractal measures and their singularities: The characterization of strange sets," *Nucl. Phys. B (Proceedings Suppl.*, vol. 2, no. C, pp. 501–511, 1987.

[42] G. Korvin, *Fractal methods in the earth science.* Amsterdam: Elsevier, 1992.

[43] R. Narayanan, M. S. Janaki, and A. N. S. Iyengar, "Fractal Dimensions of Plasma Fluctuations using Wavelet Transforms," no. 4, pp. 21–24.

[44] Evertz C J G and Mandelbrot B, *Multifractal measures Chaos and Fractals: New Frontiers of Science*. Berlin: Springer, 1992.

[45] K. Paynabar and J. (Judy) Jin, "Characterization of non-linear profiles variations using mixed-effect models and wavelets," *IIE Trans.*, vol. 43, no. March, pp. 275–290, 2011.

[46] B. M. Colosimo, Q. Semeraro, and M. Pacella, "Statistical Process Control for Geometric Specifications : On the Monitoring of Roundness Profiles," *J. Qual. Technol.*, vol. 40, no. 1, pp. 1–18, 2008.

[47] H. Lu, K. N. Plataniotis, and A. N. Venetsanopoulos, "MPCA: Multilinear principal component analysis of tensor objects," *IEEE Trans. Neural Networks*, vol. 19, no. 1, pp. 18–39, 2008.

[48] H. Lu, K. N. Plataniotis, and A. N. Venetsanopoulos, "Uncorrelated Multilinear Principal Component Analysis for Unsuper- vised Multilinear Subspace Learning," *IEEE Trans. Neural Networks*, vol. 20, no. 11, pp. 1820–1836, 2009.

[49] H. Lu, K. N. Plataniotis, and A. N. Venetsanopoulos, "A survey of multilinear subspace learning for tensor data," *Pattern Recognit.*, vol. 44, no. 7, pp. 1540–1551, 2011.

[50] Y. Chen, F. Leonelli, and H. Yang, *Heterogeneous Sensing and Predictive Modeling of Postoperative Outcomes*, no. October. 2016.

[51] G. Liu, C. Kan, Y. Chen, and H. Yang, "Model - driven Parametric Monitoring of High - dimensional Nonlinear Functional Profiles," 2014.

[52] C. Kan and H. Yang, "Dynamic spatiotemporal warping for the detection and location of myocardial infarctions," *IEEE Autom. Sci. Eng.*, no. 8th IEEE International Conference, pp. pp. 1046–1051., 2012.

[53] T. J. Vadakkan, "Multifractal spectrum of a binary image." Matlab Central 2009, 2009.